Estimating Vertical Motions in Texas via Hiatus Mapping and Flexural Backstripping

by
Nikola Bjelica

A thesis submitted to the Earth and Atmospheric Sciences,
College of Natural Sciences and Mathematics
in partial fulfillment of the requirements for the degree of

MASTER OF SCIENCE

in Geology

Chair of Committee: Lorenzo Colli

Committee Member: Jonny Wu

Committee Member: Andrew S. Madof

University of Houston
May 2022

ABSTRACT

It has been proposed that Texas experienced uplift and tilt during the latter part of the Cenozoic based on onlapping strata and truncated sequences. The precise timing, spatial extent, and amplitude of these vertical motions, as well as their dynamic causes, remain poorly constrained. We analyzed regional-scale unconformities from geologic maps and regional cross-sections of Texas to compile hiatus maps at spatial scales of many hundreds of kilometers and at temporal scales of geologic epochs. This was complemented by the analysis of subsurface geometries and by a quantitative assessment of the role of post-rift thermal subsidence and lithospheric flexure induced by sediment loading. Our analysis put additional constraints on the timing of the uplift from Upper Cretaceous through Miocene and amplitude of tilting of 650 +/- 150 meters, refining our knowledge of the tectonic history of Texas. Additionally, we were able to assess that changes in dynamic support from the convecting mantle are required to explain these past vertical motions of the Texas lithosphere.

TABLE OF CONTENTS

LIST OF TABLES

LIST OF FIGURES

INTRODUCTION

The Earth's mantle behaves like a solid over short timescales, as attested by the propagation of teleseismic transverse waves (Fowler, 2004). But on longer timescales of thousands of years or more, the mantle deforms like a fluid (Figure 1; Turcotte and G. Schubert, 2002). Heat trapped within the Earth since its formation induces vigorous thermal convection within the mantle, and more heat is constantly generated by the radioactive decay of naturally occurring isotopes of uranium, thorium, and potassium (Turcotte and G. Schubert, 2002). Unlike the pliable interior, the Earth's lithosphere, has a substantial elastic strength, which prevents it from undergoing diffuse deformation, and mantle convection instead induces plate tectonics (e.g., Davies and Richards, 1992; Davies, 1999).

Plate tectonics postulates that the lithosphere is broken into a number of rigid plates, which float and glide over the underlying mantle (Condie, 1989). Plates are internally rigid and deform only at their boundaries (Burchfiel, 1993). If two plates collide, one is forced to slide underneath the other, sinking down into the mantle (Burchfiel, 1993). But the continental crust is too buoyant and, instead of being subducted, it is folded and thrusted at the surface (Burchfiel, 1993). This deformation increases its thickness and generates mountain ranges. If, instead, two plates move apart, the lithosphere is first thinned and finally splits apart, letting new magma rise from the shallow subsurface and cool down forming fresh oceanic crust, which is thinner and denser than continental crust (Condie, 1989).

The lateral differences in the thickness and density of the crust and lithosphere caused by these tectonic processes are accommodated via flexural isostasy and are responsible for most of the Earth's relief (Turcotte and Schubert, 2014). At scales of hundreds of kilometers and greater, however, the Earth's topography is also influenced by the convective motions inside the mantle (Pekeris, 1935). This non-isostatic portion of the topography, called dynamic topography (Hager et al., 1985), is caused by the same mass anomalies that are driving mantle convection. The viscous stresses excited by mass anomalies in the mantle are transmitted to the lithosphere-asthenosphere boundary, where their normal component pushes up and pulls down the overlying lithosphere.

Dynamic topography is transient in nature, changing over millions of years following the evolution of mantle flow and it is characterized by spatial scales of 100+ kilometers and amplitudes of several hundred meters (Flament et al., 2013; Hoggard et al., 2016).

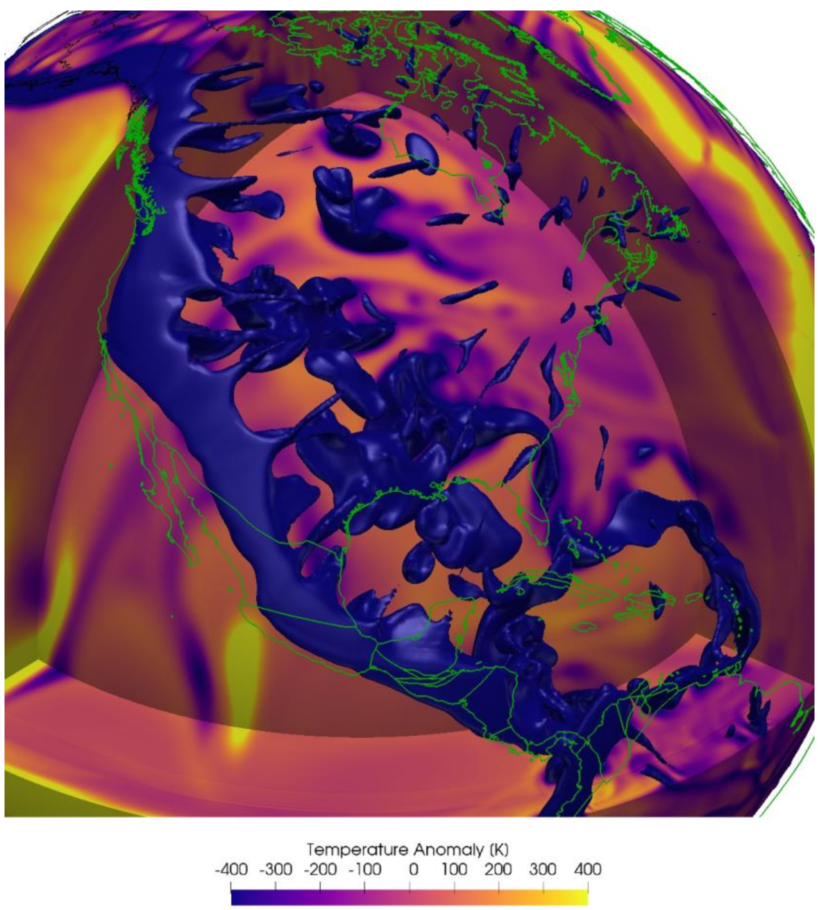

Figure 1. Temperature field underneath North and Central America*. Temperature field underneath North and Central America from a numerical model of Earth's mantle convection.*

In the Cretaceous, there existed one of the largest post-Paleozoic inland seas, which covered an area from the Arctic Ocean in the north to the Gulf of Mexico (GoM) in the south. This epeiric sea is known as Western Interior Seaway (WIS) (Slattery et al., 2015). The area covered by the WIS remained a few hundred meters below sea-level for approximately 46 million years before being uplifted, and today WIS marine sediments can be found even several hundred meters above sea-level. This uplift was not accompanied by large-scale faulting or crustal thickening, thus excluding a change in the local isostatic component of topography. The WIS is therefore the perfect example of how dynamic topography can control the available accommodation space and, through it, the evolution of paleoenvironments (Cheng and Liu, 2020).

As mentioned, the most southern portion of the WIS is connected to the GoM basin, which is located between the North American plate and the Yucatan block. The GoM started forming in the Early Jurassic with continental rifting, followed by seafloor spreading that lasted until the Early Cretaceous (Galloway et al., 2011). During the Late Jurassic through Early Cretaceous, the basin occupied by the Gulf of Mexico experienced a period of subsidence of the underlying crust due to lithospheric cooling and sediment loading (Galloway, 2008). With subsidence occurring at a faster rate than sediment could fill it, the Gulf of Mexico deepened as it expanded (Galloway, 2008).

During the remainder of the Mesozoic and throughout the Cenozoic, sediment accumulation within the GoM and its adjacent coastal plain further depressed the underlying crust (Galloway et al., 2011). The current isostatic state of the GoM, however, is not well known. Several lines of evidence point to the northeastern Gulf Coast undergoing uplift during Oligocene and Miocene (Dooley et al., 2013), which is uncharacteristic for a passive continental margin. This uplift is occurring at a much later time with respect to the rebound of the WIS, and its connection to the sinking of the Farallon plate remains poorly explored (Liu, et al., 2008) A better understanding of the history of subsidence and uplift experienced by the GoM would improve our understanding of mantle dynamics and the focus of this research will be to investigate the area south of Balcones fault zone (Figure 2).

Figure 2. Balcones fault zone. *Location of the Balcones fault zone*

The vertical motions caused by changing dynamic topography are bound to significantly influence the accommodation space for locations near sea-level, leaving a clear trace as regional patterns of deposition and erosion. Therefore, an analysis of the geologic record can provide inferences on the history of uplift and subsidence, constraining their causative dynamic processes in the mantle. Until today, this effort was hampered due to lack of investigating interregional-scale unconformities through hiatus-surface mapping as well as exploring Texas scale geologic maps as an indicator for changes in paleotopography. Quantifying how much dynamic topography has contributed to present day Texas geology is the goal of this investigation. To this extent we propose to use the Texas state geologic map to identify conformable and unconformable contacts, which will highlight missing time in the rock record (known as a hiatus) and yield the proxy records of paleotpography and vertical motions. We interpret the patterns of ongoing deposition, end of deposition, non-deposition and beginning of deposition through time and space. Additional subsurface data allows us to map such contacts into the subsurface and to constrain the large-scale layer geometries, providing additional constraints to the various potential sources of vertical crustal movements in the northwestern GoM.

METHODS

Methods for surface mapping

Building on the work done by Carena et al. (2019), we developed a method to highlight patterns of deposition and erosion, together with their evolution in time, from regional-scale geologic maps and subsurface data. The fundamental starting point is the mapping of hiatuses and conformable contacts as preserved today in the geologic record. A choice must be made regarding the time resolution at which this analysis is performed. Stratigraphic information is more abundant at coarser time resolutions (e.g., eras and periods). But the interpretability of the resulting maps is limited, because we suspect mantle dynamics to induce cycles of erosion and deposition at time periods as short as a few million years (Colli, et al., 2018). Conversely, stratigraphic information is scarcer at finer time resolutions (e.g., ages), limiting the areal extent and spatial resolution of the resulting maps. We chose to perform our analysis at the resolution of epochs, striking a balance between data availability and geodynamic relevance. We treat epochs as atomic time units, characterized by internal temporal homogeneity. The only exception will be given by Quaternary, which we will consider as an atomic unit despite being a geologic period.

We traced each chronostratigraphic unit and analyzed the contact between that unit and the one preceding it. We aimed to classify each chronostratigraphic interval either as a time of deposition or a time of non-deposition and/or erosion. A prevalence of deposition during a unit and the one preceding it would result in no hiatus and a conformable contact (at the specific time resolution used for the study). At each location in space and at each boundary in time, three other possibilities exist: beginning of deposition after a time of non-deposition or erosion; end of deposition, followed by a time of non-deposition or erosion; or ongoing non-deposition and/or erosion during both times. Notice that the beginning of deposition is associated with an unconformity (possibly paraconformity) that caps a hiatus that is resolvable at the given time resolution. The other two cases mark the formation of a hiatus but are only indirectly associated with an unconformity, as this will be formed only if deposition eventually happens at a later time.

We interpreted preserved conformable contacts as evidence of ongoing deposition across the two units. This interpretation gives a lower limit for the total area that experienced ongoing deposition at that time, as some of the sediments (and the conformable contact between them) might have been eroded later. Similarly, the presence of an unconformity is unequivocal evidence for the beginning of deposition during the chronostratigraphic unit that caps the hiatus. But in the general case, the depositional state of the missing units (during the hiatus) and of the unit below the unconformity cannot be deduced univocally from the fact that there is an unconformity, as absence of evidence is not necessarily evidence of absence. Nevertheless, our goal is to reconstruct the pattern of erosion and deposition at each time, not just the part that is currently preserved. In some cases, it is possible to arrive at a unique interpretation via logical elimination of all other possibilities. For example, when an unconformity skips only one unit. Given our assumption of internal temporal homogeneity, widespread deposition during the missing time would require those sediments to be eroded during the subsequent time. But the subsequent time must be classified as a time of deposition, as deposits are present and cap the unconformity. It follows that the missing unit (and that unit alone) must have been characterized by non-deposition and/or erosion (again, at the specific time resolution used for the study). In case an unconformity skips two or more units, only the most recent missing unit can be unequivocally assigned to a state of non-deposition or erosion.

Indeed, when we have a long-term hiatus uncertainty increases exponentially: the depositional state of each missing unit (except the most recent) is undetermined, and thus the number of possible sequences of depositional/erosional states doubles with each missing unit. As an example, suppose that at certain location Quaternary sediments lie over Paleocene sediments. We can univocally assign a non-depositional/erosional status to Pleistocene. Miocene is undetermined, and thus we have two possible states. Oligocene, too, is undetermined, and the two possible states of Miocene combine with the two of Oligocene for a total of four possible sequences of depositional statuses, which grow to eight once the uncertain status of Eocene is taken into account.

Areas where the depositional state can be constrained are denoted with a solid color (blue for ongoing deposition, purple for end of deposition, red for ongoing non-deposition/erosion and green for beginning of deposition. See Figure 3). Areas where two possibilities cannot be ruled out are filled with bands of two colors, corresponding to the two possibilities. Areas where more than two possibilities exist are colored gray.

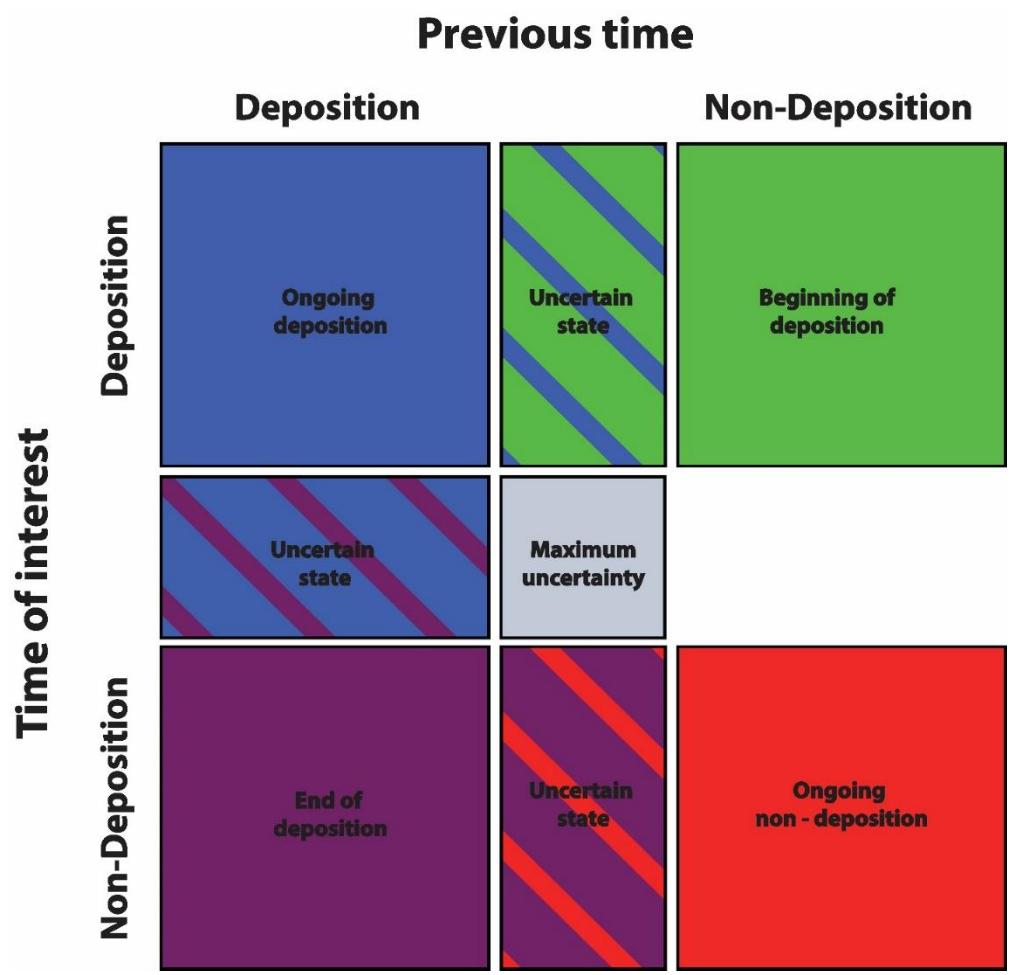

Figure 3. Mapping colors. *Five colors used in this study to highlight patterns of deposition and erosion*

We applied this method to the most updated version of the geologic map of Texas, which was prepared by the United States Geological Survey (USGS) with the cooperation of the Texas Bureau of Economic Geology from the University of Texas at Austin (Stoeser et al., 2005). The map comes as a set of four plates: Texas is divided into quadrants, with each plate showing one. It is important to note that all four quadrants are reproduced at the same scale. We uploaded all four panels in Adobe Photoshop CS6 to create a single geologic map of Texas. We used ArcGIS to georeference the combined geologic map and to make sure that all four quadrants were fitted correctly. These preparatory steps allowed us to have better constraints on mapping and more accurate interpretations.

Methods for subsurface mapping

Geologic maps summarize a large amount of information, but due to their very nature they elucidate stratigraphic contacts only where such contacts crop out to the surface. To avoid long-range extrapolations, we augmented our analysis using borehole and seismic data. These datasets also allow us to understand the geometry of the chronostratigraphic layers in the subsurface, providing additional constraints on the depositional conditions and on the history of lithospheric vertical motions, and were used to get constrains on conformable and unconformable contacts at depth.

We compiled subsurface data from the University of Texas (UT) bureau of economic geology, and the USGS subsurface database. USGS data was derived from the work done by E. T. Baker, Jr. in 1995 and it is available as open file report 94-461 and as stratigraphic and hydrogeologic work done by him in 1979 and it is available as open file report 236. The data consists of 28 cross-section lines and 463 wells. The wells range in depth from 500 to 6000 meters, and feature units from Jurassic to Quaternary in age. The work done by Kevin Mickus in 2009 and by Mark Speckien in 2012 was used for location and depth of the Moho, and for the basement we used the information from work done by John Snedden and William Galloway. We do not extend our analysis into the offshore Gulf of Mexico because we use simple model and for this study we avoid additional uncertainties and complexities of salt and listric faults.

Compiled data was first imported into ArcGIS for georeferencing. Upon that, shapefiles for cross-section lines were generated over the georeferenced locations and exported into Petrel for further analysis.

The first step in Petrel was to assure that the shapefiles were projected in the same coordinate projection as the files in ArcGIS. By doing this, we excluded location errors. Once all the shapefiles were imported in Petrel, we interpreted the tops of each epoch, going from Jurassic to Quaternary. Interpreting the tops of each epoch allowed us to create surfaces of each time of interest. Creating surfaces for each epoch made generation of isopach maps possible.

Upon completing the work in Petrel, we moved onto the final step of our investigation, quantifying thermal subsidence and lithospheric flexure effect. To do this, we used MOVE software. All the surfaces from Petrel were exported into MOVE as Zmap files.

RESULTS

Surface results

Using the methods described in the previous section, we analyzed the geologic map of Texas and the subsurface data basinward of the Balcones escarpment to reconstruct the history of deposition and sedimentation across Texas.

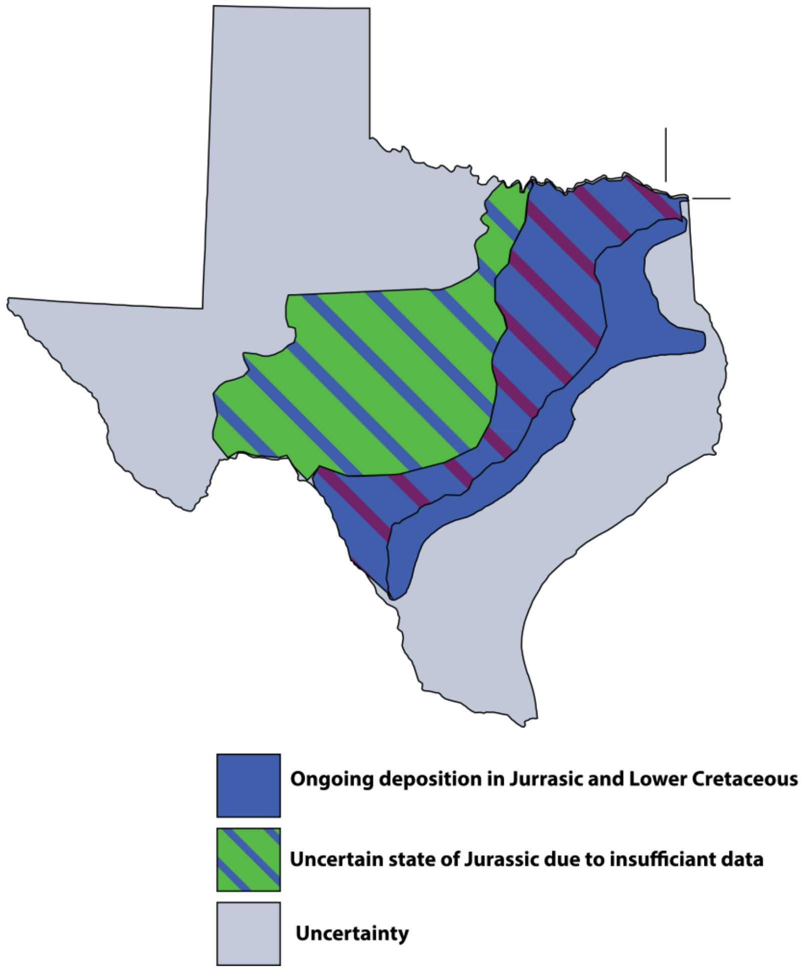

Figure 4. Base of Lower Cretaceous. *Sedimentation pattern map of base of Lower Cretaceous (145.5 Ma)*

Figure 4 shows the mapped pattern of erosion and sedimentation during the Lower Cretaceous. In the area shown in blue we have well data and regional cross-section lines that confirm the Lower Cretaceous is lying conformably over the Jurassic. Over the banded blue-green area, instead, Lower Cretaceous crops up at the surface, but we either don't have subsurface data or the data we compiled doesn't reach deep enough to discriminate what lies underneath the Lower Cretaceous. Therefore, those locations could have experienced either ongoing deposition or beginning of deposition during the Lower Cretaceous. Grey areas denote locations where three or more possibilities exist.

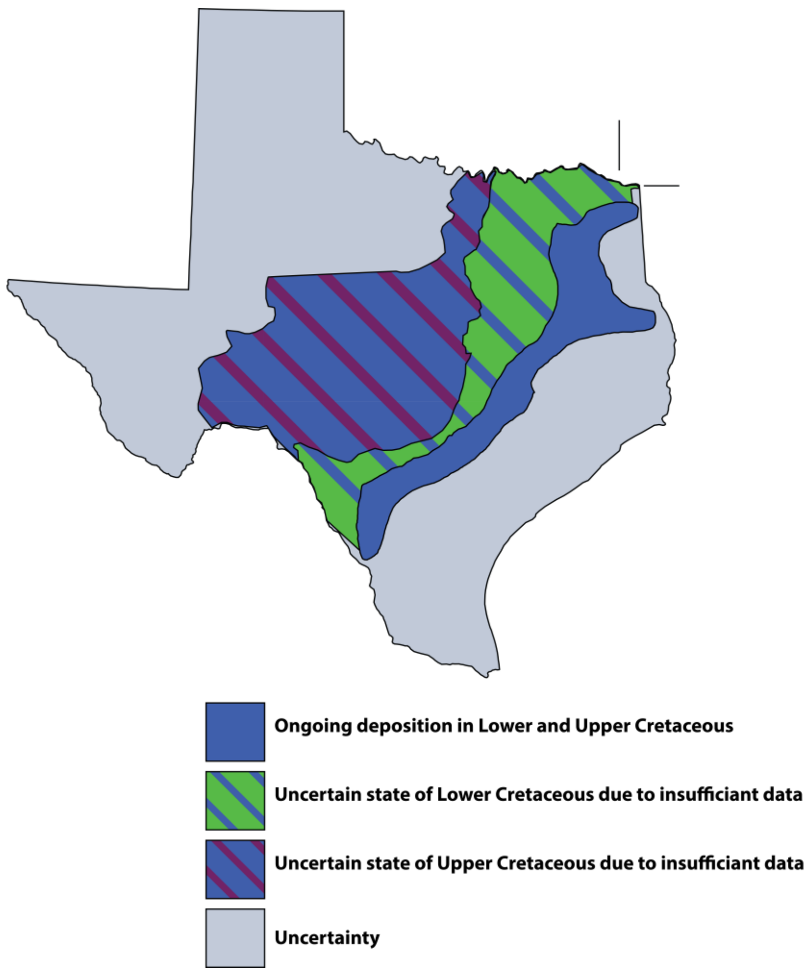

Figure 5. Base of Upper Cretaceous. *Sedimentation pattern map of base of Upper Cretaceous (100.5 Ma)*

Figure 5 shows the mapped pattern of erosion and sedimentation during the Upper Cretaceous. In the area shown in blue we have subsurface data that allows us to identify the contact between Upper Cretaceous and Lower Cretaceous at depth and that contact confirms the Upper Cretaceous is lying conformably over the Lower Cretaceous. Over the banded blue-green area, instead, Upper Cretaceous crops up at the surface, but either we don't have subsurface data or it doesn't reach deep enough to discriminate what lies underneath the Upper Cretaceous. Therefore, the state of the Lower Cretaceous remains uncertain. The area shown with purple and blue bands corresponds to where the Lower Cretaceous sediments are exposed at the surface. Currently, we don't have data to constrain whether the Upper Cretaceous sediments were deposited in this area and eroded at a later time or if they were never deposited.

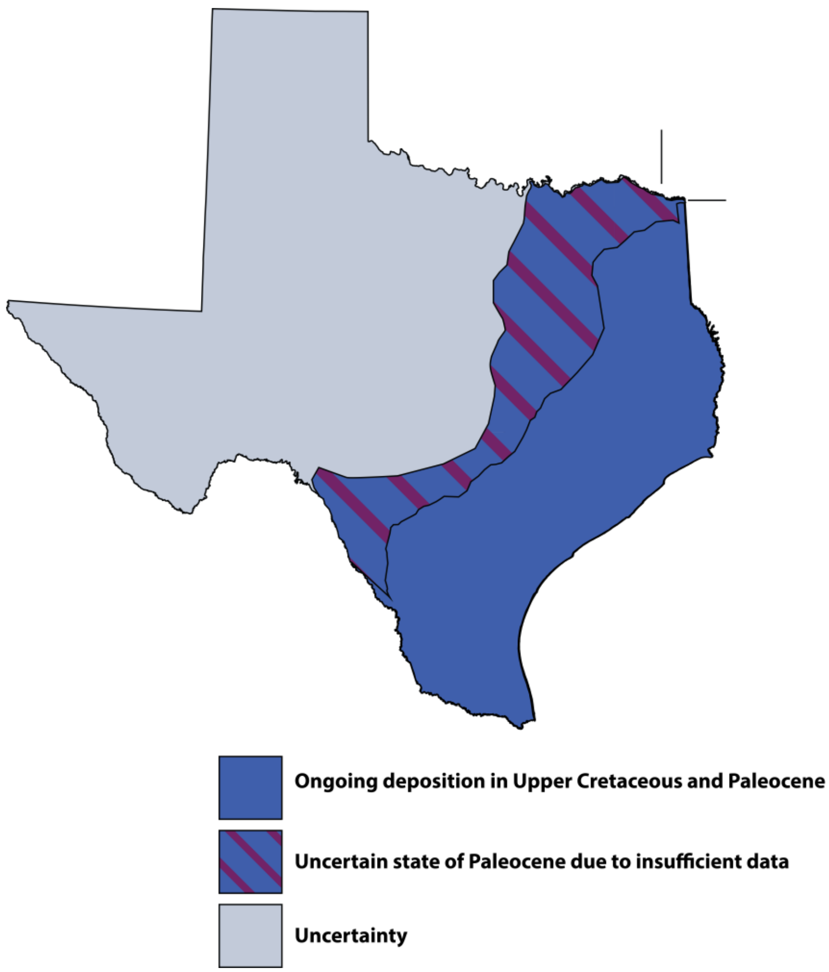

Figure 6. Base of Paleocene. *Sedimentation pattern map of base of Paleocene (66 Ma)*

Figure 6 shows our reconstruction for the base of Paleocene. The region shown in solid blue is where we can confirm ongoing deposition across the K-Pg boundary. As in Figure 5, the area shown with purple and blue bands corresponds to regions where the sediments that belong to the previous time are exposed at the surface. Therefore, we mark its state as uncertain as we cannot discriminate between deposition, erosion or non-deposition.

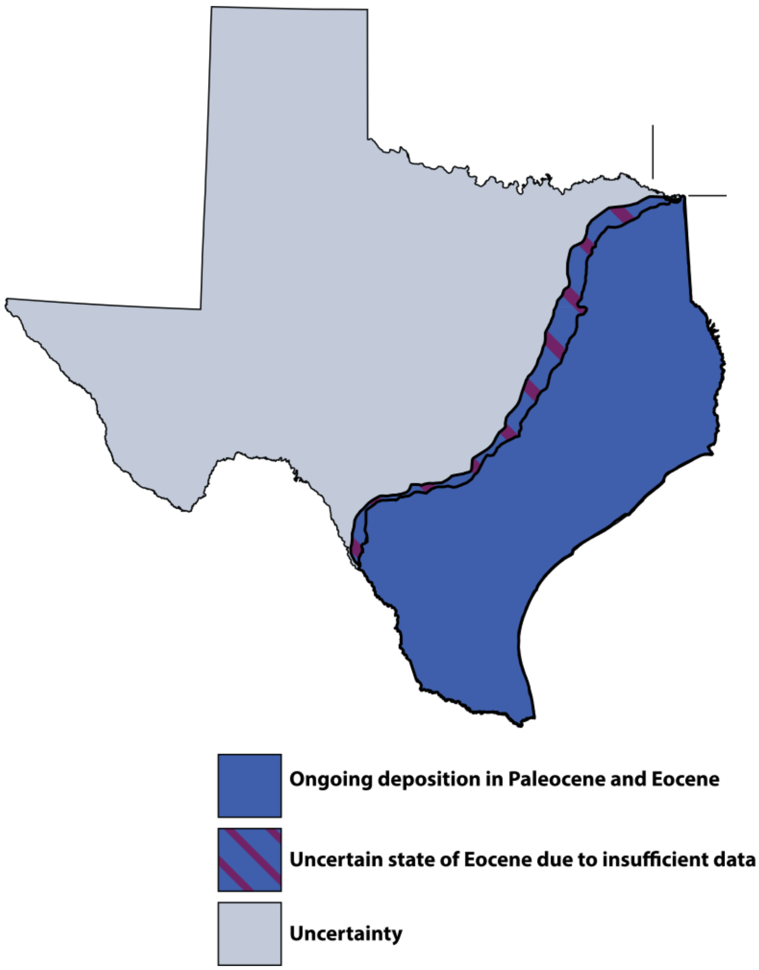

Figure 7. Base of Eocene. *Sedimentation pattern map of base of Eocene (56 Ma)*

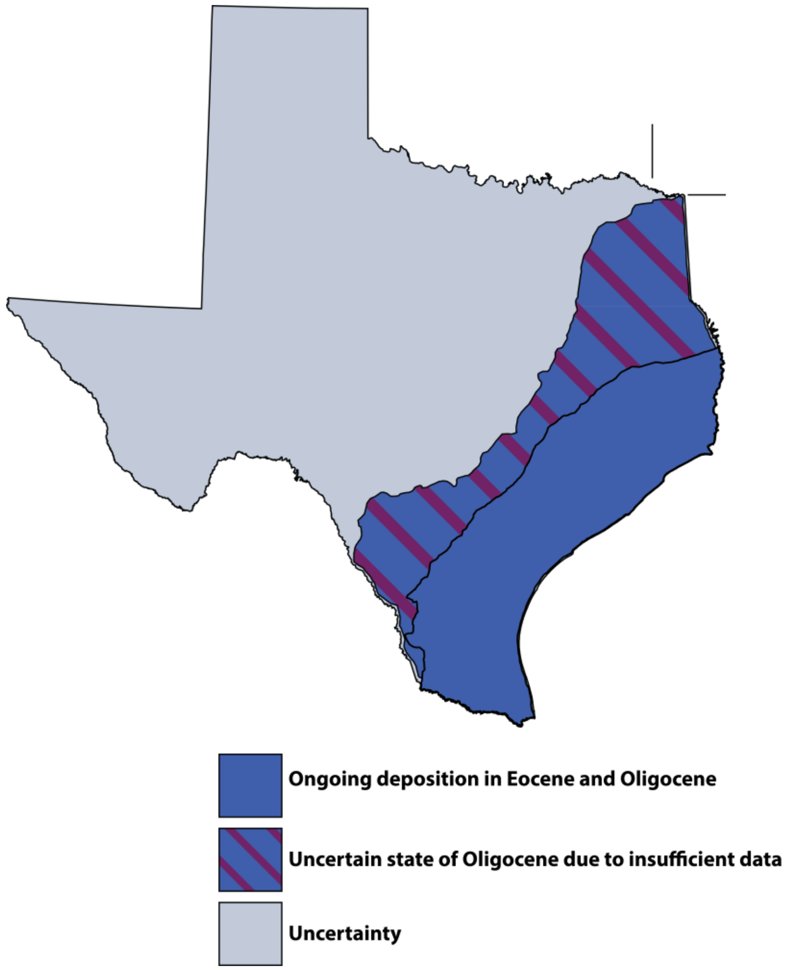

Figure 8. Base of Oligocene. *Sedimentation pattern map of base of Oligocene (33.9 Ma)*

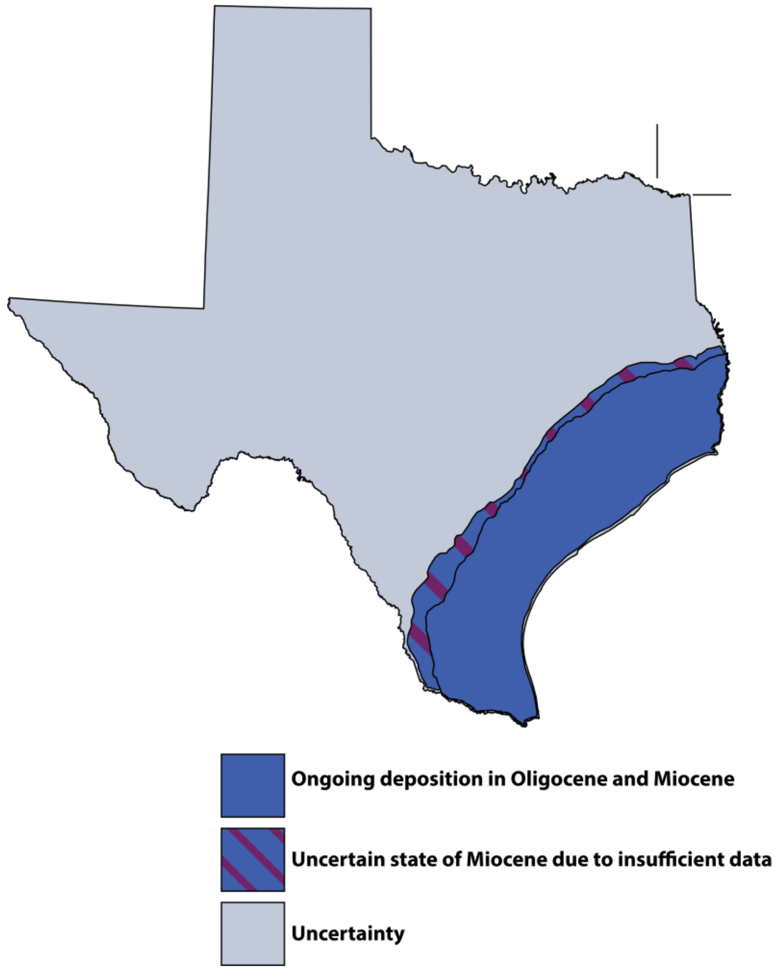

Figure 9. Base of Miocene. *Sedimentation pattern map of base of Miocene (23.03 Ma)*

Going from Eocene until Pliocene (Figures 7-9) we see that the area of confirmed ongoing deposition (based on subsurface data that allows us to see conformable contacts at depth) shrinks basinward, leaving a larger and larger area where the absence of preserved sediments of the epoch of interest and of the previous epoch prevents any inference of the past depositional state. This trend culminates in Pliocene (Figure 10), which has the smallest area (in blue) of confirmed ongoing deposition. Most of Texas was undergoing erosion or non-deposition (areas in solid purple or banded red-purple), but we cannot determine whether it was the culmination of a long-term trend of non-deposition and erosion over an ever-growing area, or if a sudden erosional event during Pliocene caused the removal of a large portion of earlier sediments from central and northern Texas.

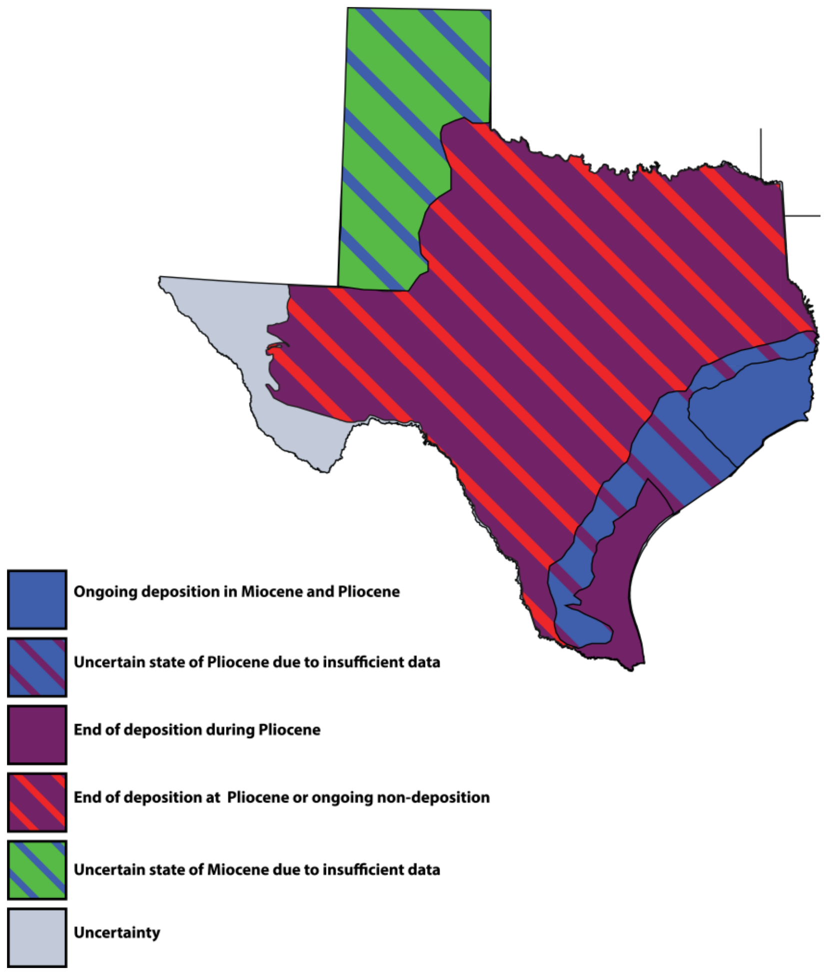

Figure 10. Base of Pliocene. *Sedimentation pattern map of base of Pliocene (5.333 Ma)*

We can exclude that Pliocene sediments were deposited and then eroded later over the area of uncertainty (purple and red) because that would require Quaternary to be a time of non-deposition and erosion; instead, there is widespread Quaternary deposition recorded over most of Texas (Figure 11).

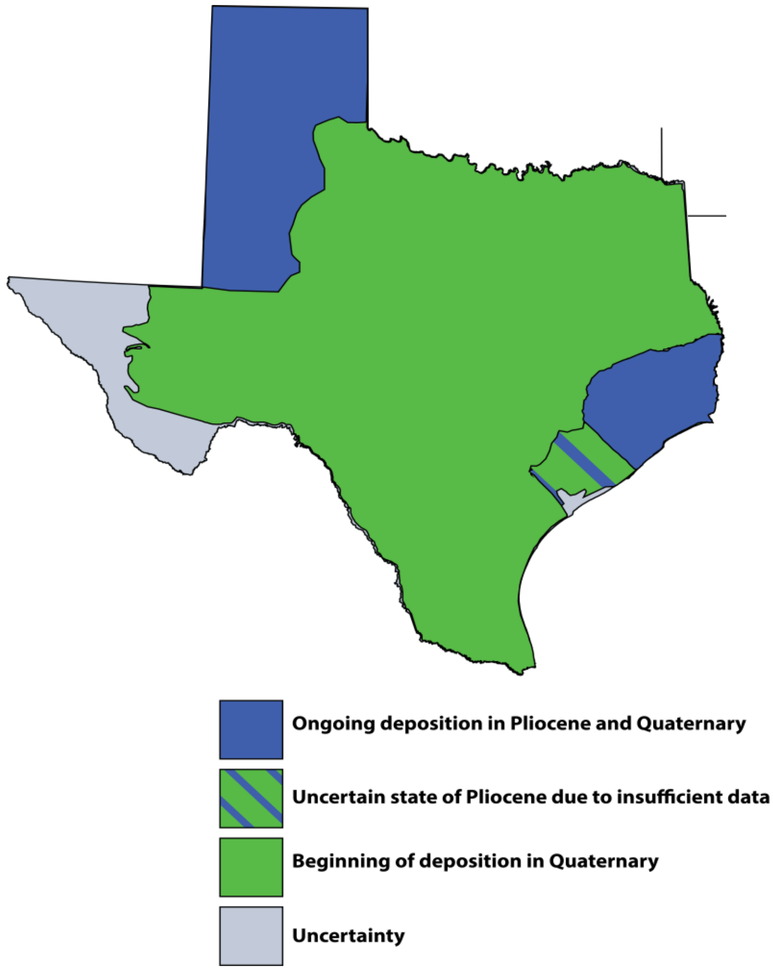

Figure 11. Base of Quaternary. *Sedimentation pattern map of base of Pliocene (2.58 Ma)*

Present-day subsurface geometries from Petrel

We imported the well data into Petrel and reconstructed the large-scale geometries of the sedimentary layers in the subsurface. We created interpolation surfaces through the depths of each stratigraphic contact across wells. All surfaces are dipping basinward, the deeper surfaces being characterized by steeper dips.

Using these surfaces, we computed the thickness of each stratigraphic layer. Maps of the thickness of each layer are shown in Figures 12–18. Lower Cretaceous, Upper Cretaceous and Paleocene have roughly uniform thickness. Eocene to Quaternary, instead, fan out basinward and become significantly thicker.

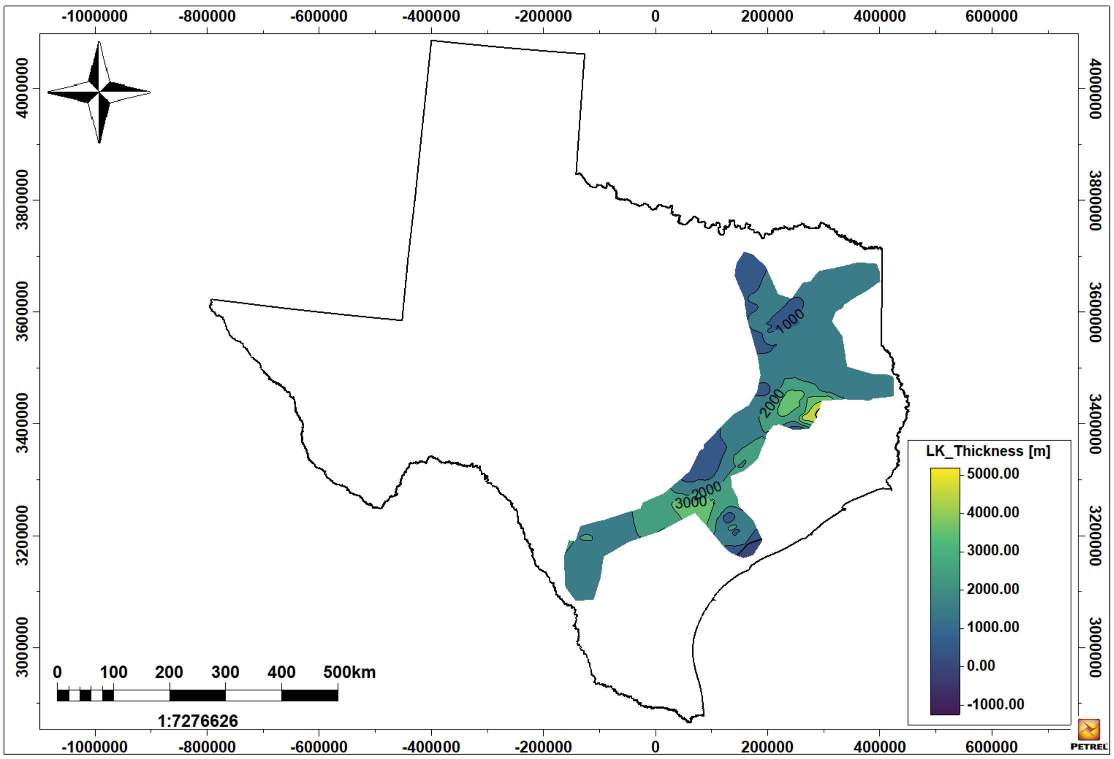

Figure 12. Lower Cretaceous isopach map. *Lower Cretaceous (145.0 Ma – 100.5 Ma) thickness map shows sediments with mainly uniform thickness throughout the entire areal extent of this map. We can't tell if sediment thickness increases basinward or stays around the same in that direction. More Jurassic sediments as well as Lower Cretaceous data is needed to get better constraints on it. There were no datasets on a regional scale available that reach depths of these sediments in this area where this map was generated.*

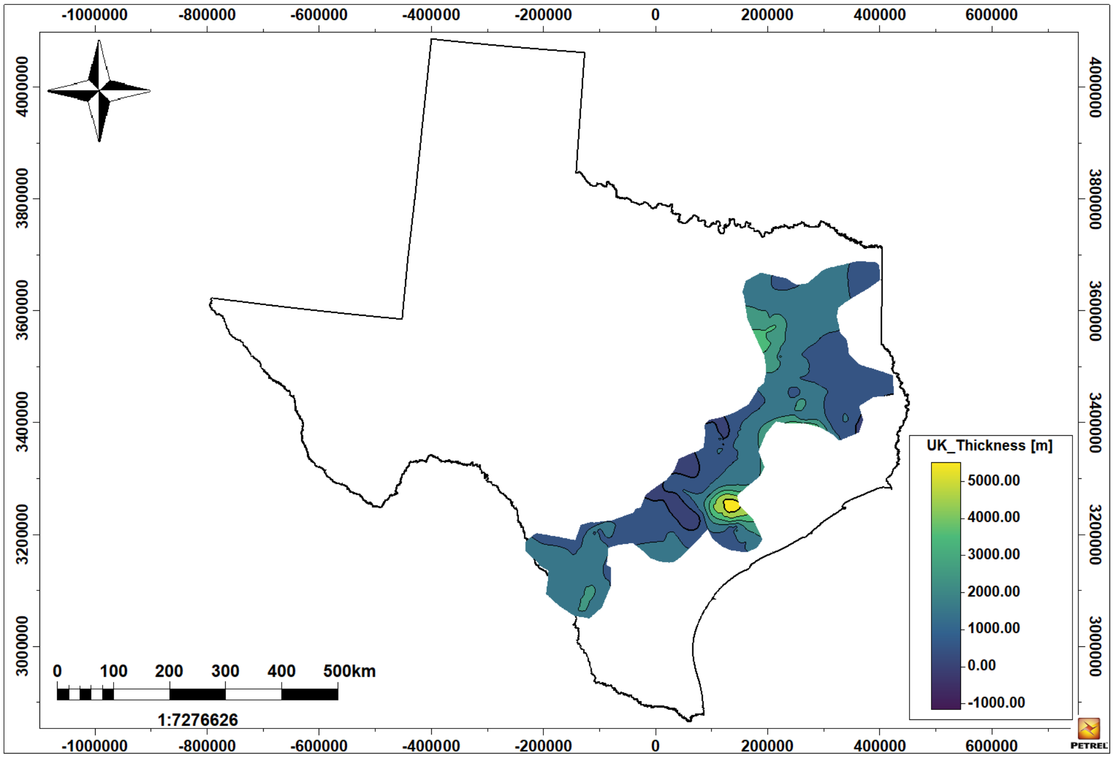

Figure 13. Upper Cretaceous isopach map. *Upper Cretaceous (100.5 Ma – 66.0 Ma) thickness map shows very similar pattern of sediment thickness as Lower Cretaceous where uniform thickness is present uniformly all over the mapped area.*

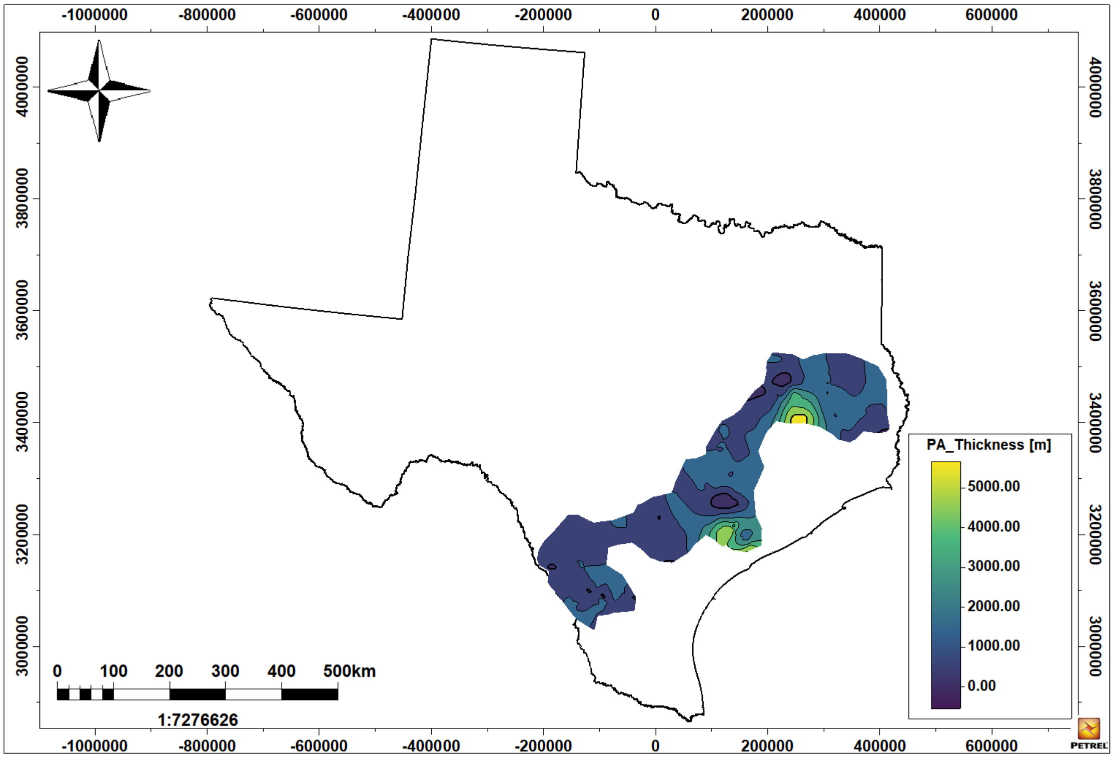

Figure 14. Paleocene ispoach map. *Paleocene (66.0 Ma – 56.0 Ma) thickness map similar patterns like Lower Cretaceous and Upper Cretaceous sediments. Small areas in northeastern part and in the central part of the map show thickness increase basinward. More Upper Cretaceous data is needed in order to get better understanding of the Paleocene sediments if the increase their thickness basinward or not. Problem with Cretaceous sediments is explained in the previous two figures.*

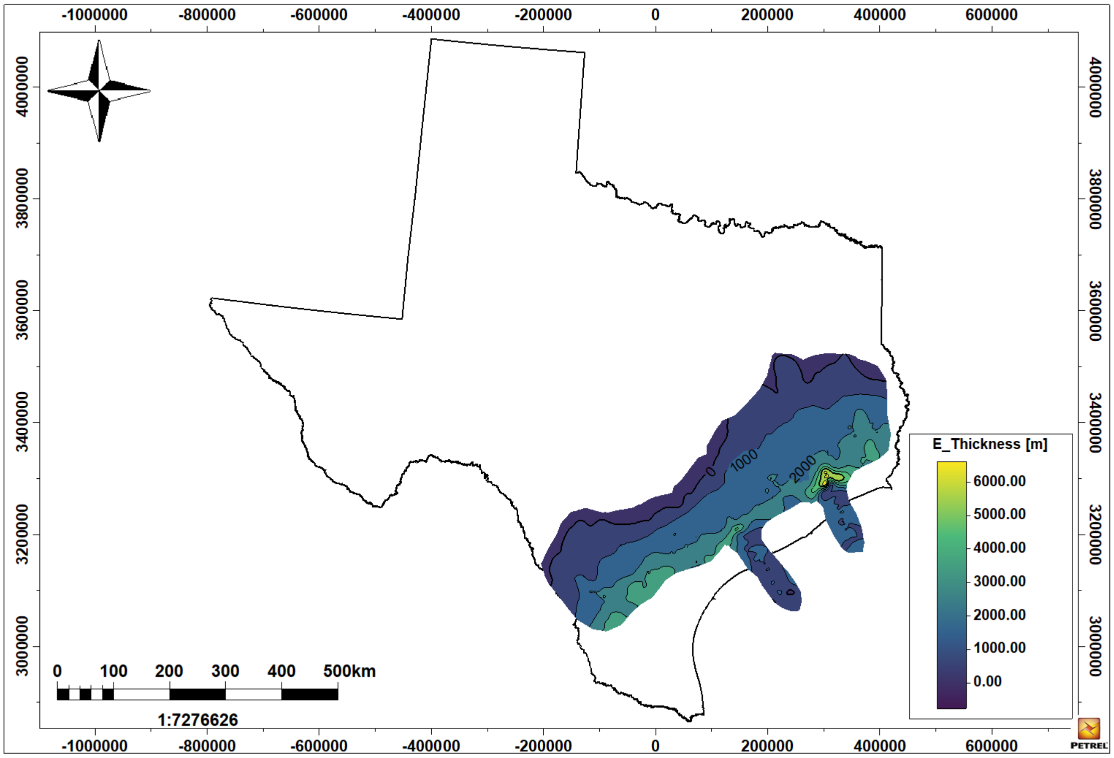

Figure 15. Eocene isopach map. *Eocene (56.0 Ma – 33.9 Ma) sediment thickness. In general, the sediment package thickens to the southeast. We observe sediment thickness basinward, with maximum thickness occurring in the northern and southern regions toward the basin.*

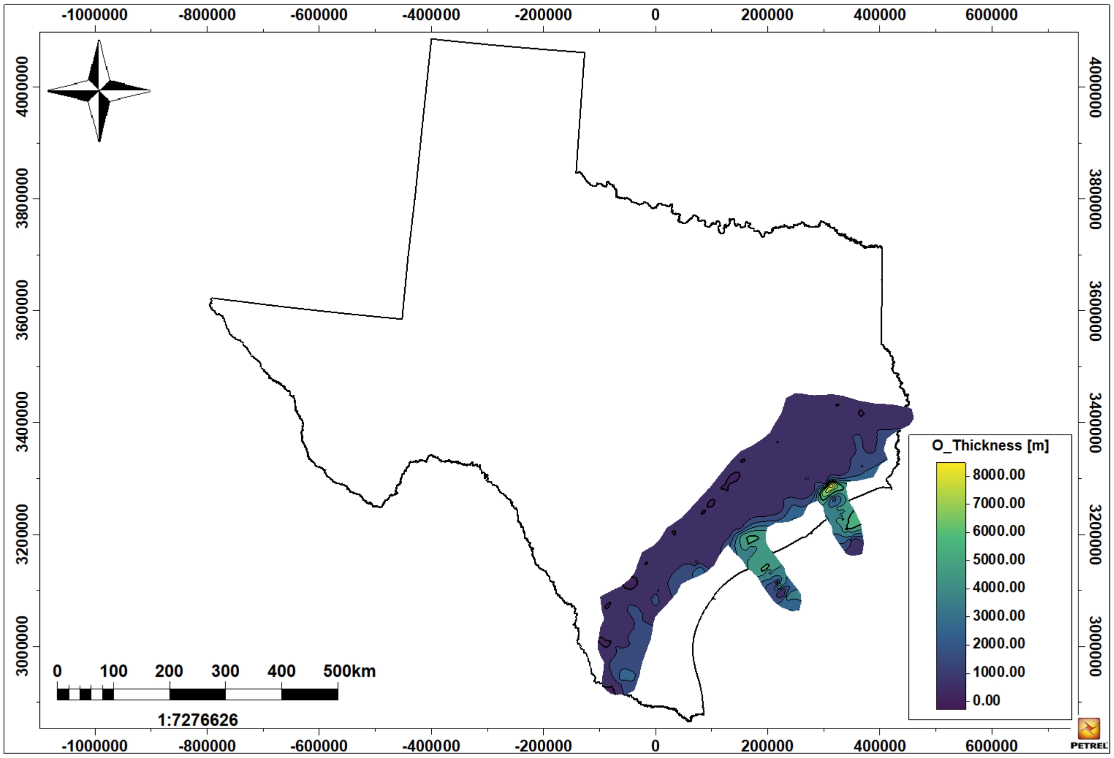

Figure 16. Oligocene isopach map. *A map of Oligocene (33.9 Ma – 23.03 Ma) sediment thickness. The general trend is the same as the Eocene, but the total sediment thickness is lower.*

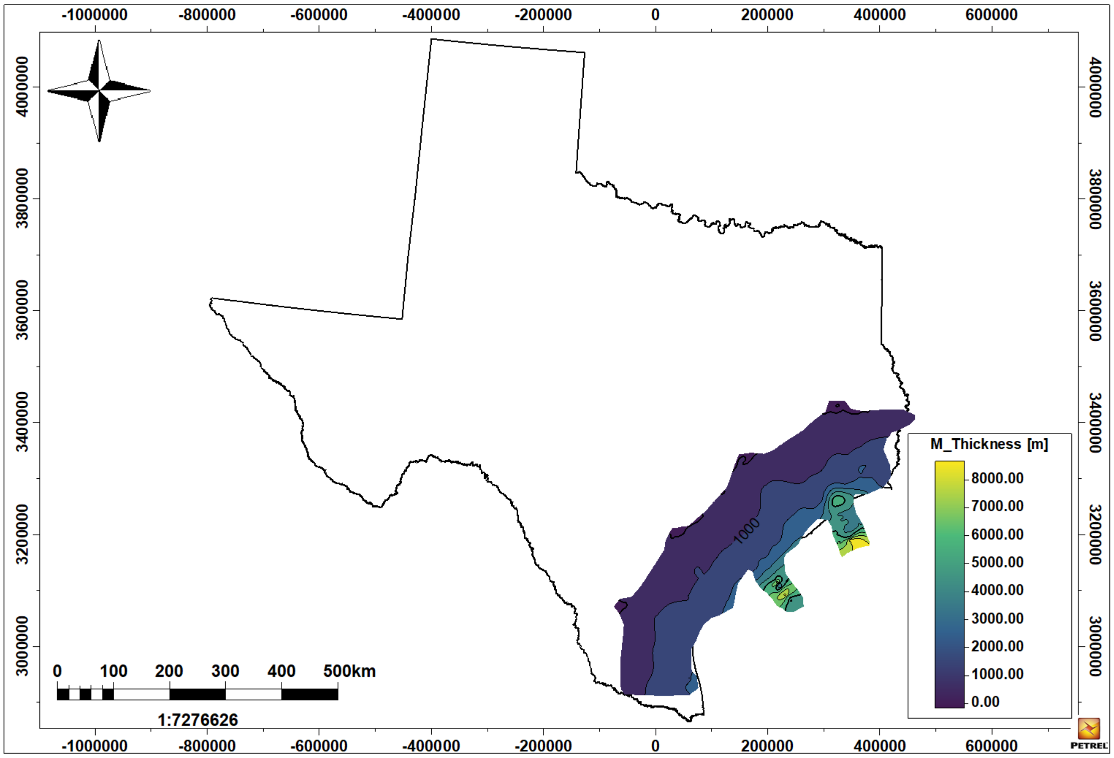

Figure 17. Miocene isopach map. *A map of Miocene (23.03 Ma – 2.58 Ma) sediment thickness. General trend is followed in the Miocene as well, as sediment thickness map shows the same patterns observed in the Eocene and Oligocene epochs with sediments being thicker in the northeastern part of the map.*

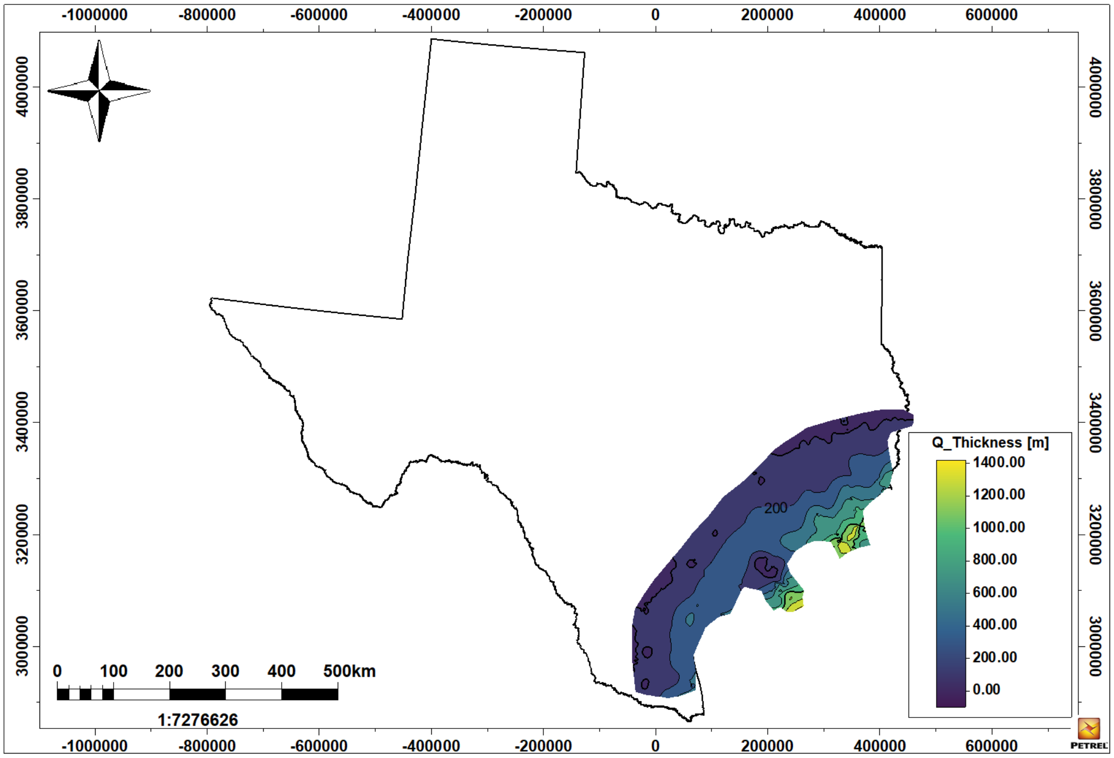

Figure 18. Quaternary isopach map. *A Quaternary sediment thickness map. The sediment thickness follows the same trend as the previous epochs. The Quaternary has the smallest total sediment thickness.*

Flexural backstripping results using MOVE

As our final step, we performed a flexural backstripping of the post-rift sequence of sedimentary layers to quantitatively investigate the potential for long-term dynamic uplift or subsidence of the Texas platform. We imported the layer geometries over a coast-perpendicular cross-section (Figure 19) from Petrel into MOVE as Zmap files. We characterized the lithology of each layer, together with their density, porosity and elastic parameters, using published databases and well logs (Baker, 1995; Baker, 1979; Snedden and Galloway, 2019; Mickus, et al., 2009; Speckien et al., 2012). We assume that rifting started at

215 Ma and lasted for 50 Myr (Dr. Magdalena Curry, personal communication). We estimated the syn-rift crustal extension from the regional cross-sections of (Snedden and Galloway, 2019; Mickus, et al., 2009; Speckien et al., 2012). We assume a homogeneous equivalent elastic thickness of 15 km. The software MOVE is designed to sequentially remove each sedimentary layer back in time, computing corrections for flexural isostatic movements, sediment compaction and thermal subsidence.

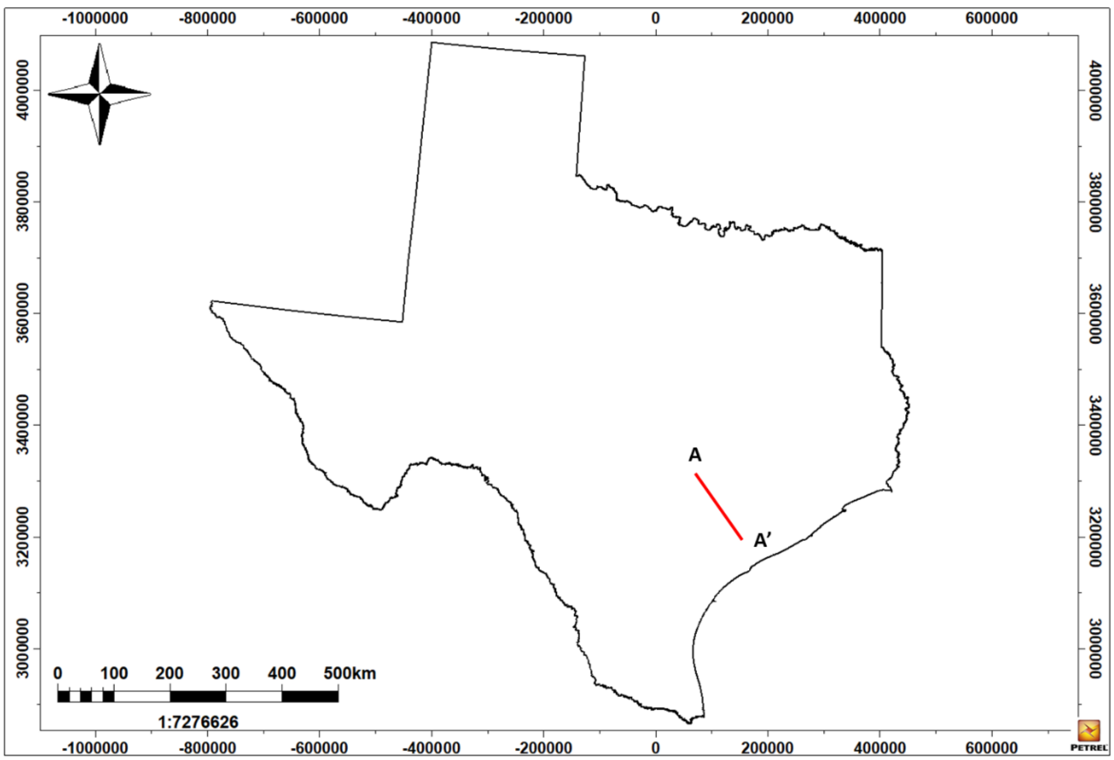

Figure 19. MOVE cross-section line location. *The location of the cross section line used for this study. Detailed investigation of this line is shown in the next 35 figures, 7 tables and 1 graph*

The resulting flexurally backstripped cross-sections over the Epochs are reported in Figures 20-24. They are all vertically exaggerated to the maximum available in MOVE (VE=25x) for better view. Figures showing the cross-sections with no vertical exaggeration are in the appendix. We compare the modeled paleoshoreline against paleoshorelines reconstructed from the geologic record (Snedden and Galloway, 2019), which are marked as crosses in the figures.

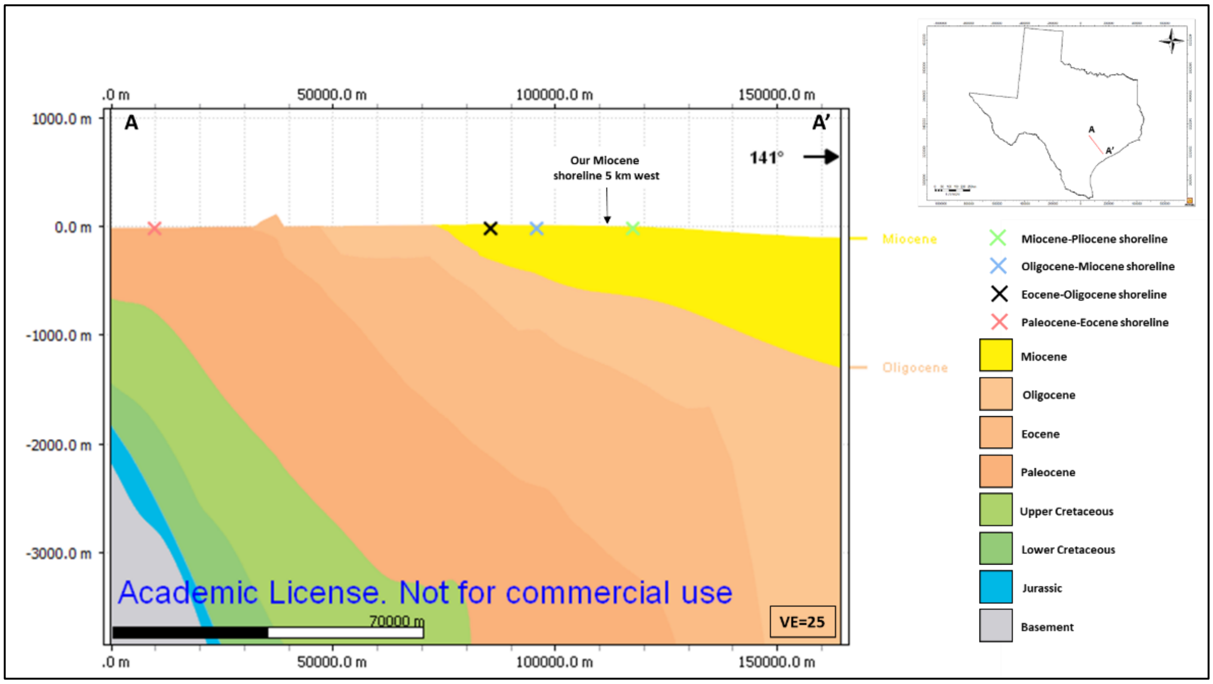

Figure 20. Model 1 Miocene-Pliocene boundary. *Cross-section showing Miocene-Pliocene boundary after decompaction of Quaternary and Pliocene sediments. For this model we used 215 Ma for rifting age, 50 Ma for syn-rift duration and 15 km for elastic thickness. These parameters apply for figures 20 to 24. Refer to table 1 and graph 1 for the results. Red crosses in this figure (and all the others after this one) represent paleo-shorelines. The first red cross on the left represents Paleocene-Eocene shoreline, the second from the left is Eocene-Oligocene shoreline, the third is Oligocene-Miocene shoreline and the fourth one is Miocene-Pliocene shoreline. After decompacting Quaternary and Pliocene we found Miocene-Pliocene shoreline to be 5 km to the left of the observed shoreline.*

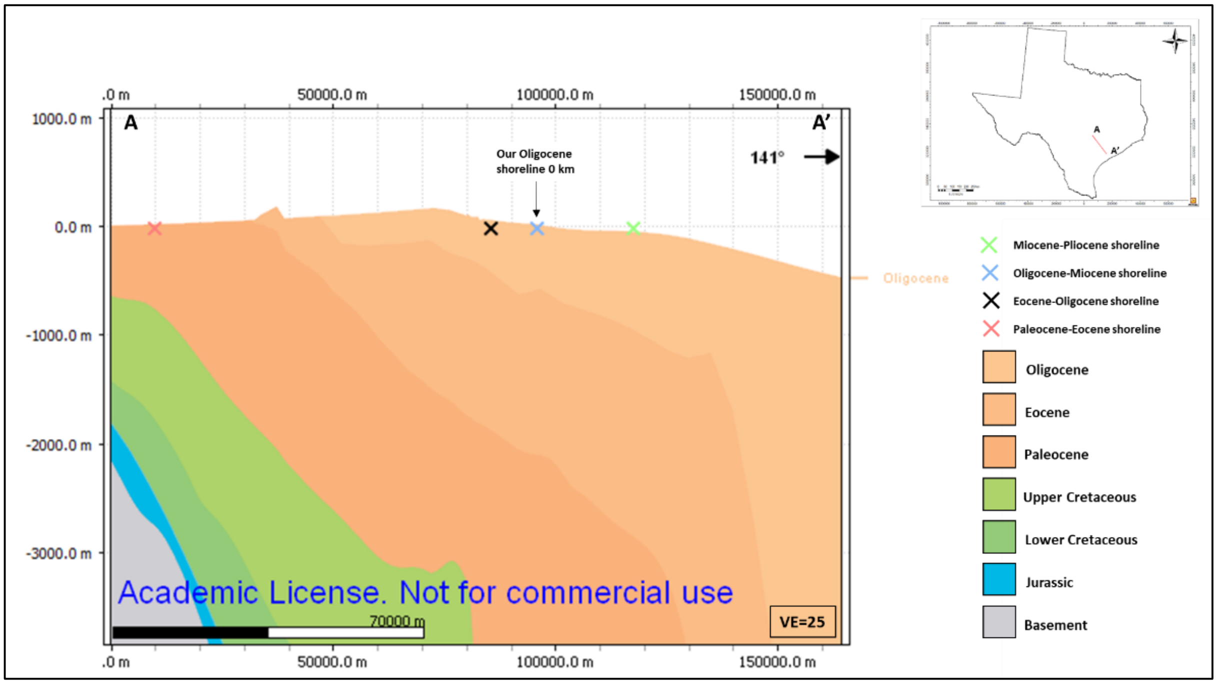

Figure 21. Model 1 Oligocene-Miocene boundary. *Cross-section showing Oligocene-Miocene boundary after decompaction of Miocene sediments. After decompacting Miocene, we found Oligocene-Miocene shoreline to be at the exact same location as the observed one.*

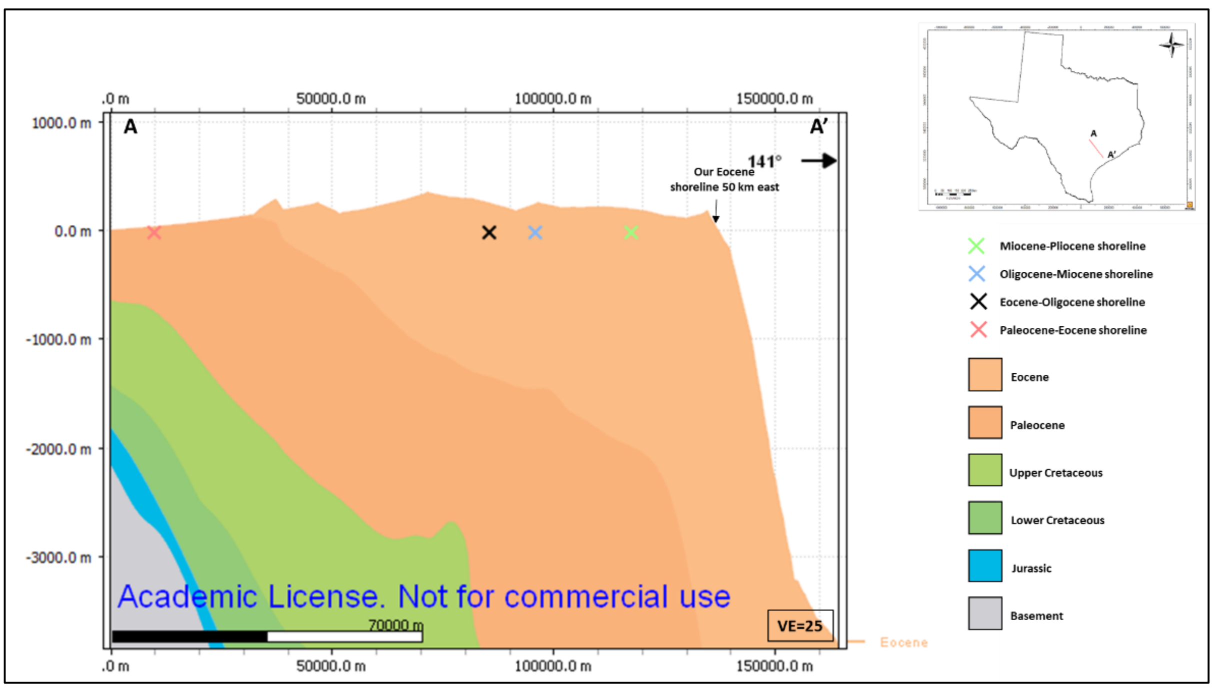

Figure 22. Model 1 Eocene-Oligocene boundary. *Cross-section showing Eocene-Oligocene after decompaction of Oligocene sediments. After decompacting Oligocene, we found Eocene-Oligocene shoreline to be 50 km to the east of the observed shoreline.*

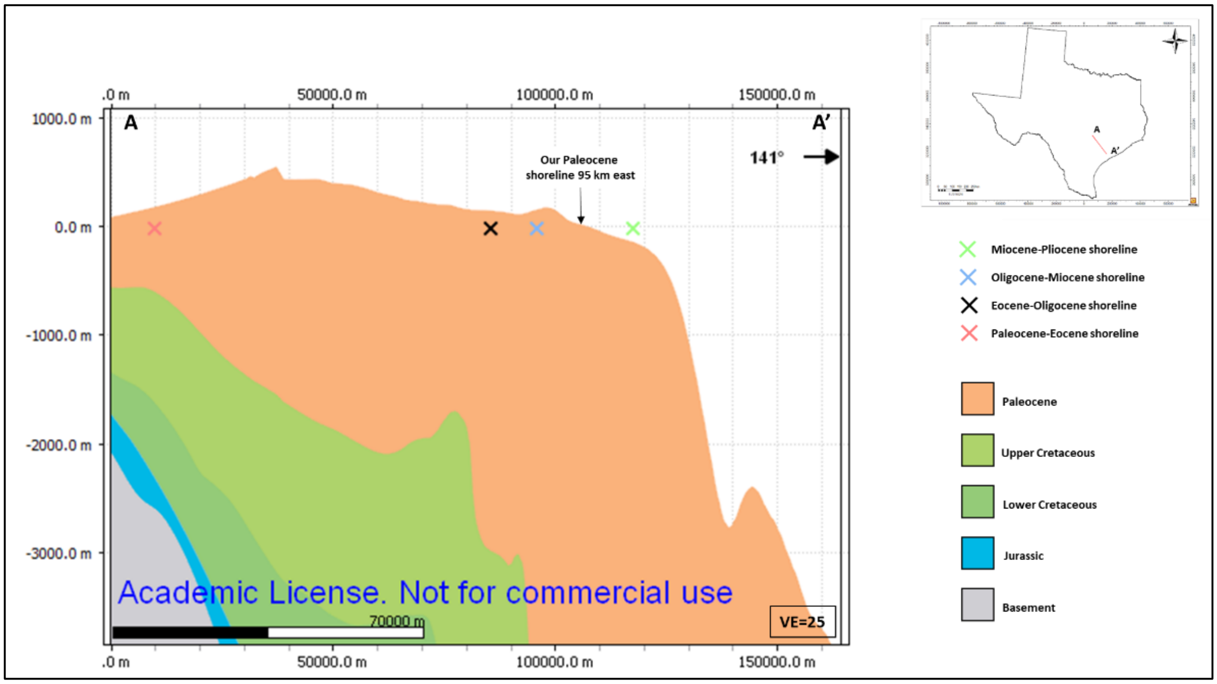

Figure 23. Model 1 Paleocene-Eocene boundary. *Cross-section showing Paleocene-Eocene boundary after decompaction of Eocene sediments. After decompacting Eocene, we found Paleocene-Eocene shoreline to be 95 km to the east of observed shoreline.*

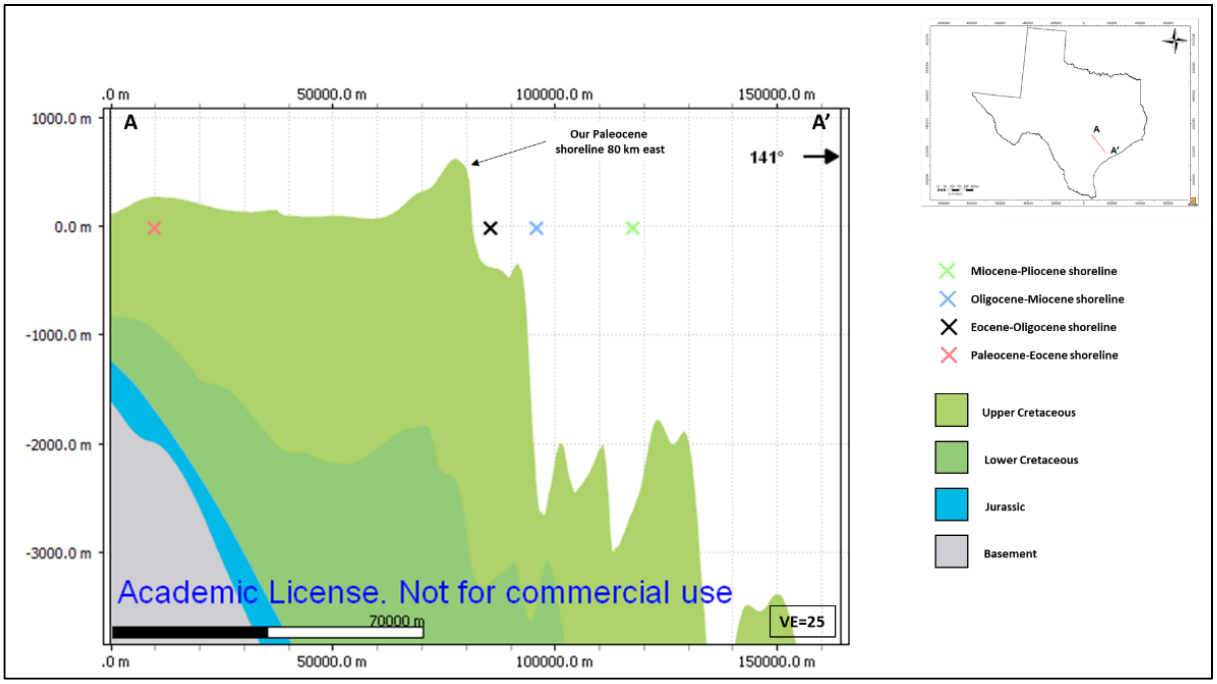

Figure 24. Model 1 Upper Cretaceous-Paleocene boundary. *Cross-section showing Upper Cretaceous-Paleocene boundary after decompaction of Paleocene sediments. After decompacting Paleocene, we found Upper Cretaceous-Paleocene shoreline to be at 80 km to the east of observed shoreline.*

While the modeled paleotopography is reasonable for the recent past, going further back in time the paleotopography is reconstructed too high and the paleoshoreline is reconstructed several tens of km basinward. The maximum discrepancy is obtained for the Upper Cretaceous, which is reconstructed several hundred meters above sea level, with a shoreline at 80 km on the cross-section. We know that at that time Texas was well below sea level, with the actual shoreline being in New Mexico. These results are summarized in Table 1.

In order to assess how dependent these results are on our choices for the various modeling parameters, we ran six other models where we varied the equivalent elastic thickness, the rifting time and the lithologies of all layers. These parameters are summarized in Table 1.

Two models have a larger equivalent elastic thickness of 30 and 60 km. Two models have an instantaneous rifting at 215 Ma and 166 Ma. One model changes the lithology of all layers increasing shale (the lithology with the largest compaction) by 20%, removing it preferentially from limestone (the lithology with the smallest compaction). If limestone constitutes less than 20%, the remainder is removed from sandstone. The final model mirrors the previous one, increasing limestone and decreasing shale by 20%.

Table 1. Seven models*. Summarized results from all the models shown here. Model 2 through model 7 is in the appendix.*

		Model 1 - Reference	Model 2 - Stronger lithosphere	Model 3 - Strongest lithosphere	Model 4 - Early instantaneous rifting	Model 5 - Late instantaneous rifting	Model 6 - Shale biased	Model 7 - Limestone biased
rifting time [Ma]		215	215	215	215	166	215	215
syn-rift duration [Ma]		50	50	50	0	0	50	50
Equivalent elastic thickness [km]		15	30	60	15	15	15	15
Lithology		standard	standard	standard	standard	standard	+ 20% shale	+20% limestone
Distance from paleo-shoreline [km]	Miocene	15 west	20 west	30 west	30 west	10 west	15 west	0
	Oligocene	0	5 wets	10 west	5 west	0	0	0
	Eocene	50 east	25 east	5 east	50 east	50 east	50 east	50 east
	Paleocene	95 east	70 east	60 east	90 east	95 east	90 east	95 east
	Upper K	80 east	55 to 80 east	40 east	50 to 80 east	80 east	80 east	80 east
Highest elevation [m]	Miocene	40	40	30	80	40	35	40
	Oligocene	180	190	160	170	180	180	190
	Eocene	370	450	430	320	370	380	360
	Paleocene	550	800	790	440	520	500	500
	Upper K	630	750	790	500	630	730	590

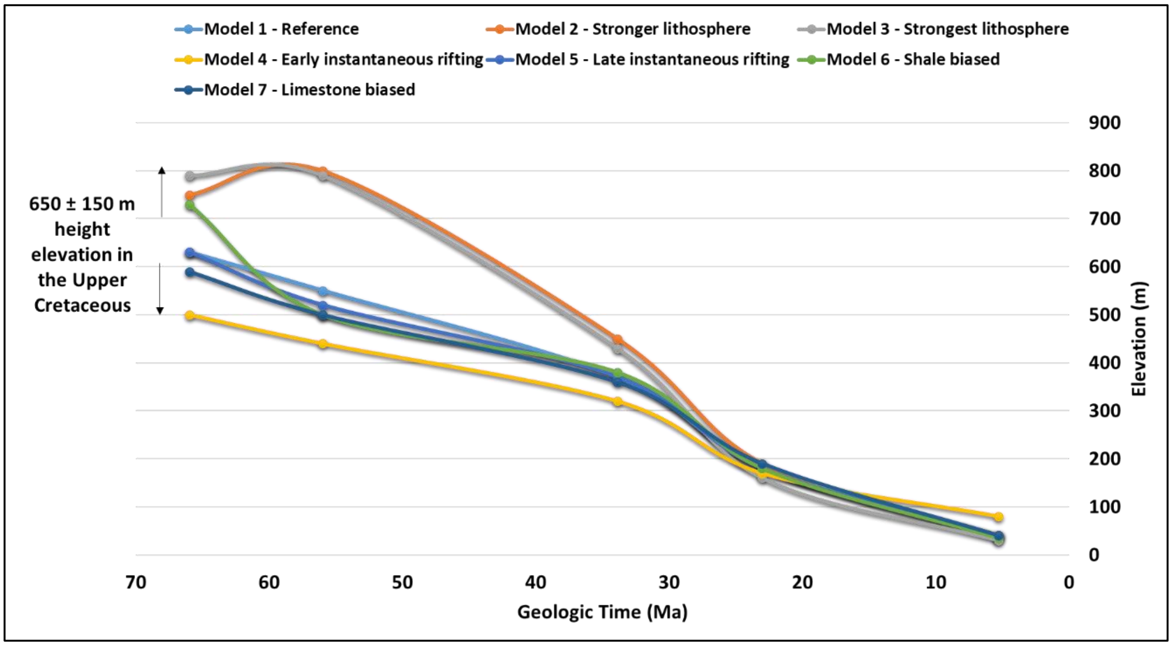

Figure 25. Summary of all seven models. *Maximum paleotopographic elevation against time for all seven models is plotted in this figure. Our results show that Texas platform was dynamically depressed by 500-800 m with respect to today and that Texas platform was dynamically uplifted between Upper Cretaceous and today. Our reconstructed elevations are 500-800 m above sea level which are unaccounted for by flexural isostasy and thermal subsidence.*

DISCUSSION

While a lot of effort has been dedicated to understanding vertical motions connected with structural deformation at plate boundaries, much less attention has been paid to episodes of long-wavelength vertical motions not caused by faulting. Our pioneering work is the first of its kind for the Gulf Coast. We have developed a new approach to map and interpret regional-scale stratigraphic contacts to investigate long-term trends in deposition and erosion. These can be interpreted as proxies for variations in accommodation space, and thus vertical land motion relative to sea level. This approach can be most successfully applied to tectonically quiet regions, which limit the confounding influence of local erosional and depositional events associated with fault movements.

Our hiatus mapping results show evidence for widespread erosion at least during Pliocene (Figure 10), with the possibility of erosion and non-deposition starting already in the Paleocene in north Texas and expanding basinward over time (Figures 4 - 9). We interpret this as evidence for large-scale uplift, certainly during the Pliocene and possibly extending over most of the Cenozoic. The depositional pattern and the subsurface geometry (Figures 3D geometries) are suggestive of a margin-wide tilt towards the southeast. The available geologic evidence documents a low-relief Texas platform that is fully marine during the Cretaceous, slowly emerging over time as the coastline moves basinward. Flexural backstripping, however, reconstructed the Texas platform at higher elevations back in time (Figure backstripping line plot), culminating in an elevation of 650 ± 150 m in the Cretaceous. Our sensitivity analysis shows that uncertainties in the timing and evolution of rifting, in the flexural rigidity of the lithosphere and in the lithology of the sedimentary layers do not affect significantly the overall uplift over time.

To reconcile this result with the overwhelming evidence of Texas being below sea level at that time, we need to invoke some additional process(es) that depressed the Texas platform by at least 650 m. If this non-isostatic depression had remained constant up to today, the Upper Cretaceous sediments would be 650 m deeper than they currently are, and the present-day coastline would be in central Texas. The basinward migration of paleoshorelines can be matched only if this non-isostatic depression (with respect to present day) during Cretaceous times got lifted up over time. Having only one paleobathymetric control point at each time interval prevents us from assessing whether this non-isostatic uplift was uniform, or if there was basinward tilting. The most straightforward candidate process is the dynamic topography associated with the subduction of the Farallon plate (Liu, et al., 2008), which could have easily caused the Texas platform to be dynamically depressed by 500 to 800 meters in the Upper Cretaceous. The subsequent sinking of the Farallon plate would have reduced its influence at the surface, reducing the dynamic depression over time until today.

In performing our flexural backstripping, we have not considered two factors: salt tectonics and fault activity. Assessing quantitatively salt deformation over time is a very complex task. Unlike most other sedimentary formations, salt deforms as a fluid. Consequently, it leaves only limited geologic traces that can be used to constrain its kinematics. In particular, it is not known how much salt was present in the study area, how much salt moved out of our study area basinward, nor how much has been dissolved. We intentionally limited the lateral extent of the cross-section we used for flexural backstripping to exclude the area where significant salt is present today. However, any amount of Jurassic Louann salt that needs to be retrodeformed landward would cause thickening of the sedimentary package back in time and, even accounting for flexural isostatic compensation, would necessary lead to an additional increase in elevation (going back in time) in our study area. Therefore, salt tectonics do not trade off with dynamic topography.

Several coast-parallel normal faults characterize the coastal plains of Texas. These are thought to be caused by gravitational sliding of sediments into the GoM, and to be linked via listric faults to deepwater thrust-and-fold belts. Unlike salt tectonics, fault activity can in principle be reconstructed with a fair degree of accuracy if seismic stratigraphy and well data of sufficiently high quality is available, particularly in depositional settings such as a continental passive margin. Unfortunately, we didn’t attempt because it was outside the scope of the project, and therefore couldn’t account for fault kinematics in our flexural backstripping. However, we can carry out here the same argument as for salt tectonics: retrodeforming these normal faults would increase the reconstructed thickness of sedimentary layers in our study area, causing larger elevation values.

The temporal resolution of our analysis is another outstanding issue. From a geophysical perspective it would be natural to analyze depositional sequences with a uniform timescale. This would require sampling at a temporal rate small enough to capture the highest significant frequencies and avoid aliasing (using e.g. a Nyquist criterion). The time series would then be suitably filtered in order to focus on the timescales of interest, which in our case are several millions of years and longer. But this is impractical for two fundamental reasons. On the one hand, deposition is a highly variable and discontinuous process across many spatial and temporal scales. This is reflected on the structure of sedimentary layers, which are frequently fractal all the way down to scales of a few millimeters. This poses a big challenge for the representation and analysis of a temporal sequence with the usual tools of real analysis. This issue compounds with the difficulty and laboriousness of measuring absolute ages of rocks, in particular the depositional age of sedimentary rocks. This is made worse by the amount of dating measurements implied by the regional scope of this study. The available subsurface data is thus primarily lithostratigraphic, with only a few chronostratigraphic tie points at depth. The temporal resolution of our analysis had to follow these constraints. Geologic ages would be the closest to the ideal few-to-several Myr resolution. But we had to settle for Epochs as they provide the best trade-off between availability, uncertainty and relevance for our goals. Adhering strictly to Epochs would cause the duration of our time intervals to range from a maximum of 45 Myr for the Lower Cretaceous to a minimum of 12 kyr for the Holocene. We thus decided to keep Quaternary undifferentiated, raising the minimum duration to the 2.58 Myr of the whole Quaternary. Two considerations are in order. First, both

Quaternary and Pliocene are still quite a bit shorter than all other intervals, Oligocene and Paleocene being the next shortest at about 10 Myr. Considering Quaternary and Pliocene together would balance the timescale but would require merging Epochs across a Period boundary. A second issue is given by the very nature of the Quaternary, which marks the beginning of northern hemisphere glaciation cycles, with the Holocene being the latest interglacial. The signal highlighted by the base of Quaternary hiatus map of renewed deposition after a period of erosion may therefore be predominantly due to the Earth currently being close to a glacial minimum and thus a maximum of relative sea level.

Our research was focused on the part of the Gulf Coastal Plain that is located south of the Balcones fault, and it consisted of interpretations of preserved sediments at the surface and in the subusurface. Constraints on if, when, where and how much erosion occurred in the past can in principle be estimated using other geological and geophysical methods, such as low-temperature thermochronology, geomorphic analysis and inverse modeling of river profiles. These methods would also complement the paleobathymetry constraints that can be gleaned from subsurface data, and would thus help in exploring the possibility of a large-scale tilt of the Texas platform.

CONCLUSION

We developed seven two-dimensional regional scale flexural isostasy models that incorporate varying elastic thicknesses, rifting initiations, syn-rift duration and varying lithologies to investigate the dynamic component of uplift impacting deposition through time on epoch scales. Our results suggest that the Texas platform has experienced a dynamic uplift since the Upper Cretaceous of 650 ± 150 m that cannot be easily explained by flexural isostasy and thermal subsidence. The best current explanation is that we are seeing the rebound from a state of dynamic depression caused by slowdown and cessation of subduction at the Western margin of North America.

BIBLIOGRAPHY

Baker, E. T., Stratigraphic and hydrogeologic framework of part of the coastal plain of Texas, Texas department of water resources, Austin, TX, 1979

Baker, E. T., Stratigraphic nomenclature and geologic sections of the Gulf Coastal Plain of Texas, U.S. Geological Survey, Austin, TX, 1995

Burchfiel, C. B., Proceedings of the American Philosophical Society, v. 137, pp. 1-29, 1993

Carena, S.; Bunge, H.P.; Friedrich, A. M., Canadian Journal of Earth Sciences, v. 56, pp. 1333-1346, 2019

Cheng, C.; Liu, L., The Geological Society of America, v. 133, pp. 347-361, 2020

Condie, C. K., Plate tectonics and crustal evolution, Pergamon Press, Tarrytown, NY, 1989

Colli, L.; Ghelichkhan, S.; Bunge, H.-P.; Oeser, J., Gondwana Research, v. 53, pp. 252-272, 2018

Davies, F. G.; Richards, A. M., The Journal of Geology, v. 100, pp. 151-206, 1992

Davies, F. G., Dynamic earth: plates, plumes and mantle convection, Cambridge University Press, New York, NY, 1999

Dooley, T. P.; Jackson, M. P. A.; Hudec, M. R., AAPG Bulletin, v. 97, pp. 1737-1764, 2013

Flament, N.; Gurnis, M.; Muller, R. D., Lithosphere, v. 5, pp. 189-210, 2013

Galloway, W. E.; Miall, A. D., The Sedimentary Basins of the United States and Canada, Elsaveir, Amsterdam, The Netherlands, 2008

Galloway, W. E.; Whiteaker, T. L.; Ganey-Curry, P. Geosphere, v. 7, pp. 938–973, 2011

Hager, B. H.; Clayton, R. W.; Richards, M. A.; Comer, R. P.; Dziewonski A. M., Nature, v. 313, pp. 541-545, 1985

Hoggard, M. J.; White, N.; Al-Attar D., Nature Geoscience, v. 9, pp. 456-463, 2016

Liu, L.; Spasojevic, S.; Gurnis, M., Science, v. 322, pp. 934-937, 2008

Mickus, K.; Stern, R. J.; Keller, G. R.; Anthony, E. Y., Geology, v. 37, pp. 387-390, 2009

Pekeris, C. L., Geophysical Journal International, v. 3, pp. 343-367, 1935

Slattery, J. S.; Cobban, W.A.; McKinney, K.C.; Harries, P.J.; Sandness, A.L., Wyoming Geological Association Guidebook, v. 32, pp. 22-60, 2015

Snedden, J. W.; Galloway, W. E., The Gulf of Mexico sedimentary basin: Depositional evolution and petroleum applications, Cambridge University Press, New York, NY, 2019

Speckien, M.; Dunbar, J.A.; Pulliam, J., Magnetic investigation of the continental-oceanic crustal boundary in the northern Gulf of Mexico, ProQuest, Ann Arbor, MI, 2012

Stoeser, D.B.; Green, G.N.; Dumonceaux, G. M.; Heran, W.D., A Digital Geologic Map Database for the State of Texas: U.S. Geological Survey Data Series, 2005

Turcotte, D. L.; Schubert, G., Geodynamics, Cambridge University Press, Cambridge, United Kingdom, 2002

Turcotte, D. L.; Schubert, G., Geodynamics, Cambridge University Press, Cambridge, United Kingdom, 2014

APPENDICES

APPENDIX TITLE: Figures of the remaining six models

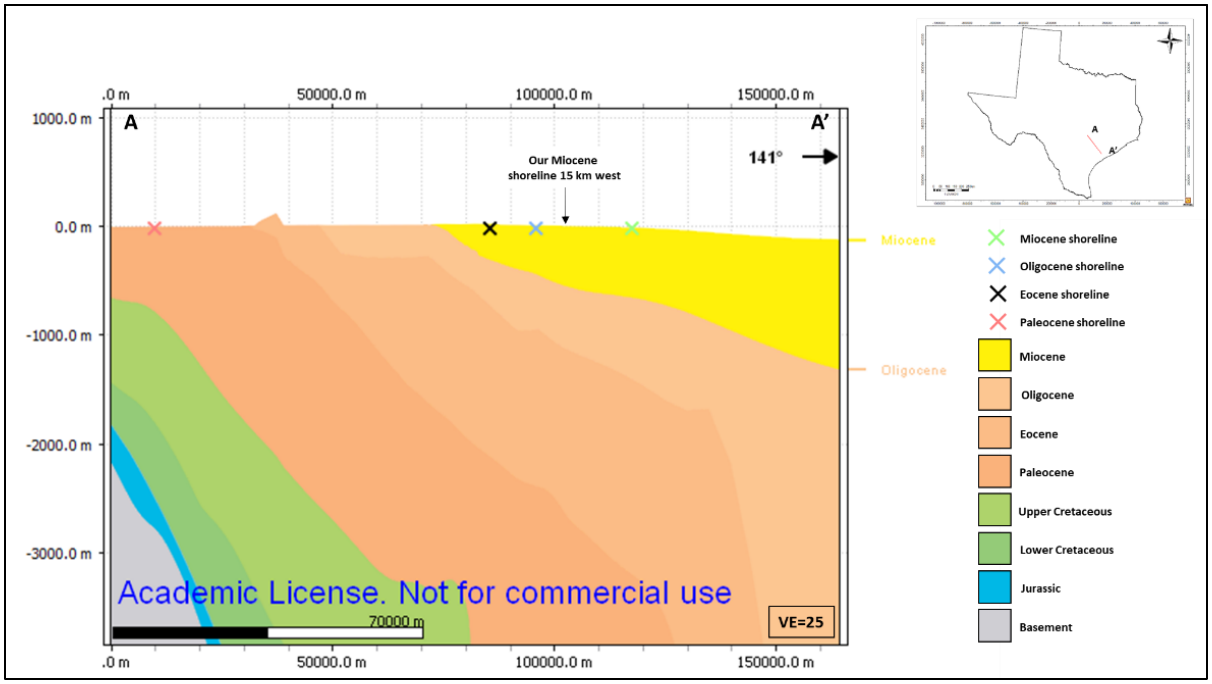

Figure 26. Model 2 Miocene-Pliocene boundary. *Cross-section showing Miocene-Pliocene boundary after decompaction of Quaternary and Pliocene sediments. For this model we used 215 Ma for rifting age, 50 Ma for syn-rift duration and 30 km for elastic thickness. These parameters apply for figures 26 to 30. Refer to table 1 and figure 25 for the results.*

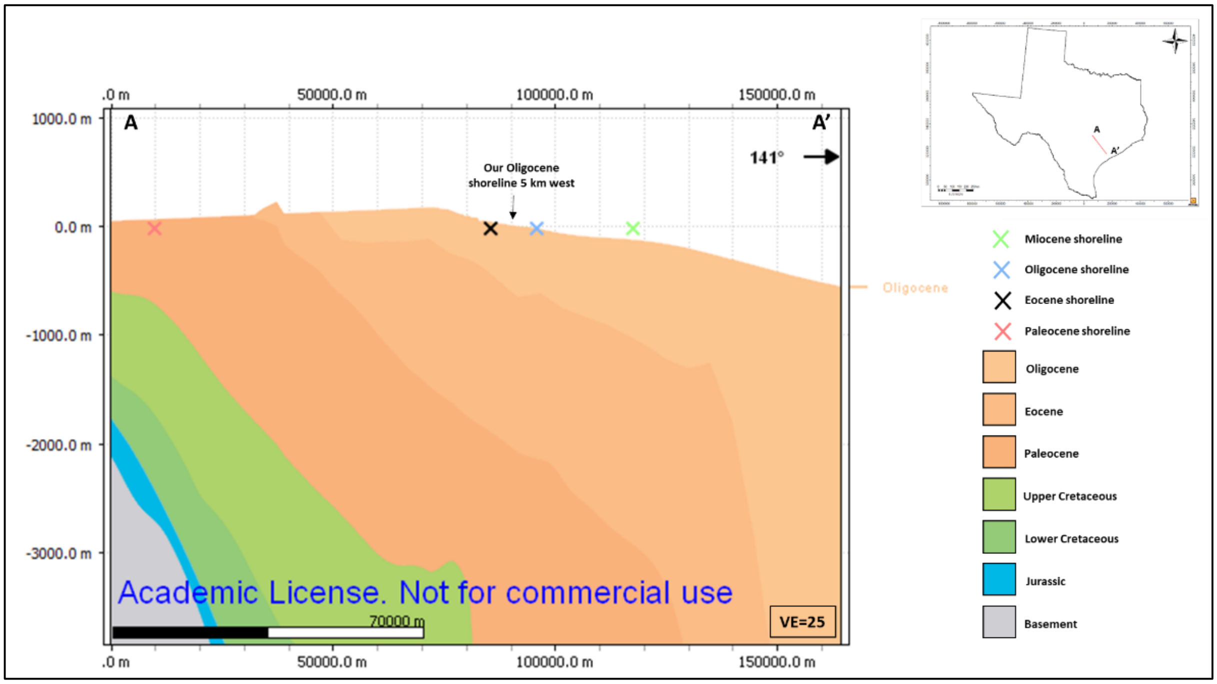

Figure 27. Model 2 Oligocene-Miocene boundary. *Cross-section showing Oligocene-Miocene boundary after decompaction of Miocene sediments.*

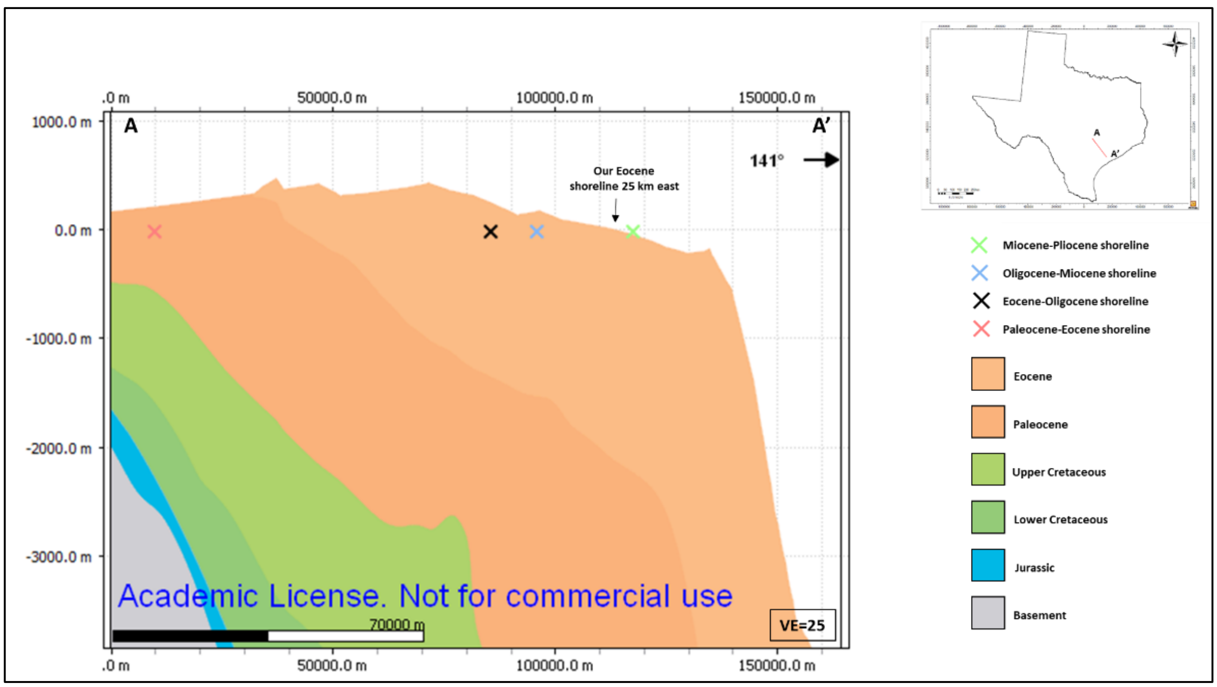

Figure 28. Model 2 Eocene-Oligocene boundary. *Cross-section showing Eocene-Oligocene after decompaction of Oligocene sediments.*

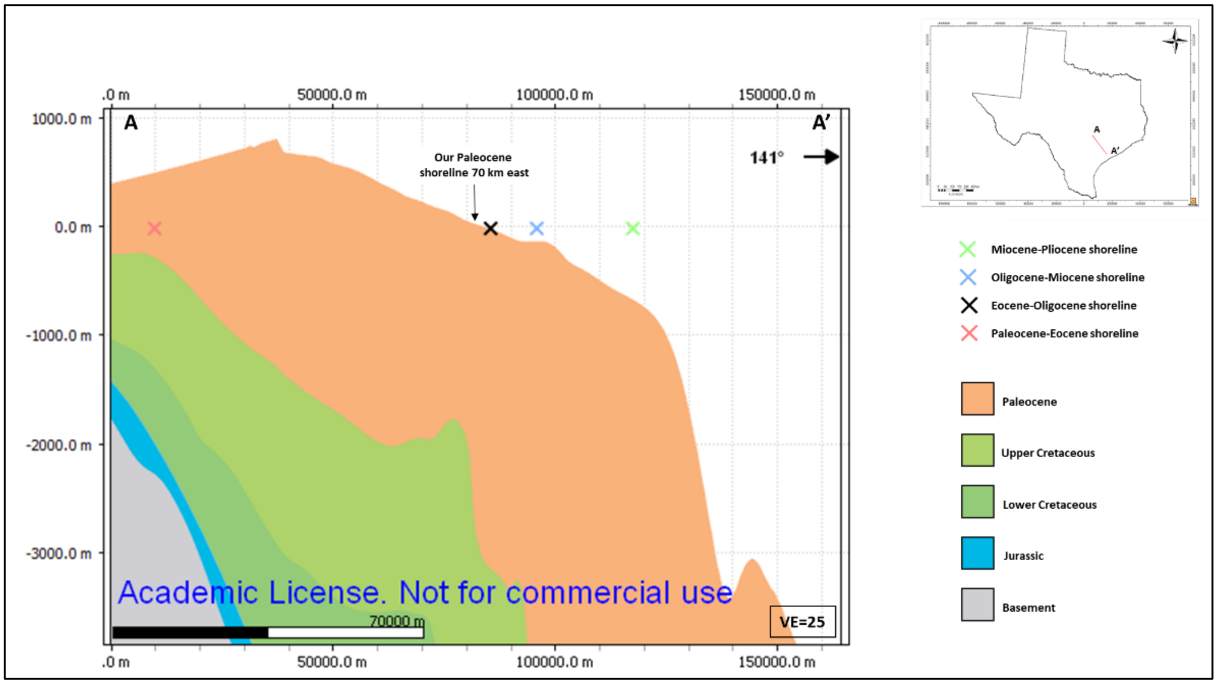

Figure 29. Model 2 Paleocene-Eocene boundary*. Cross-section showing Paleocene-Eocene boundary after decompaction of Eocene sediments.*

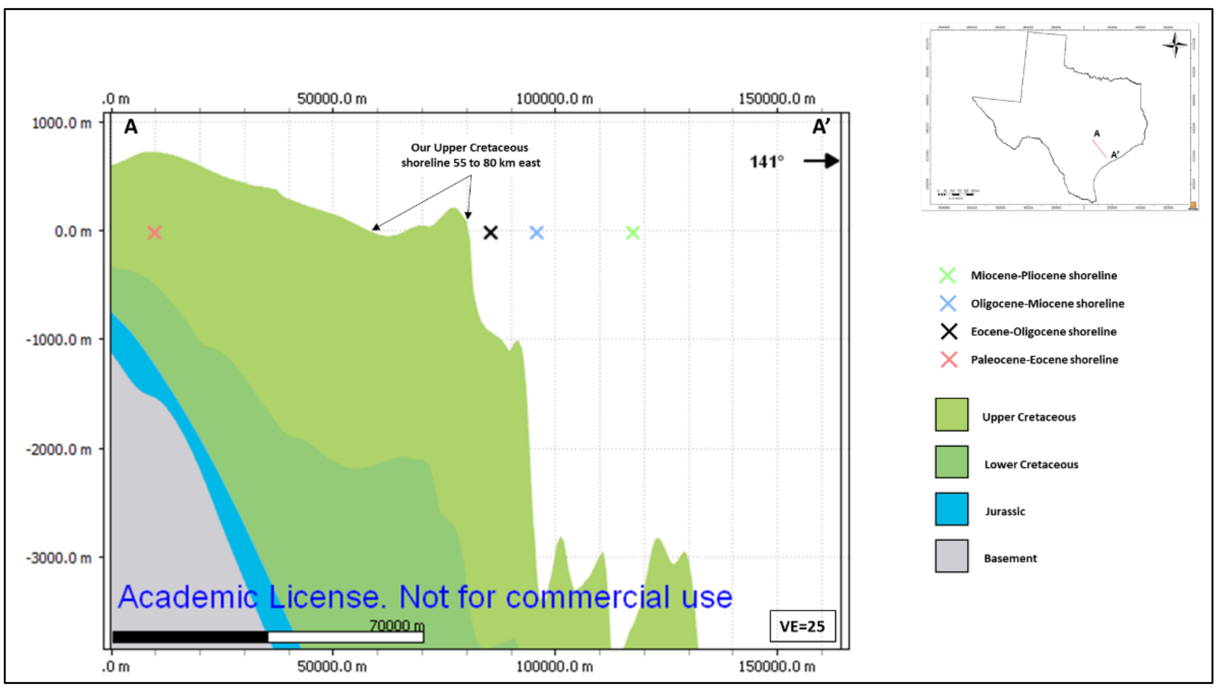

Figure 30. Model 2 Upper Cretaceous-Paleocene boundary. *Cross-section showing Upper Cretaceous-Paleocene boundary after decompaction of Paleocene sediments.*

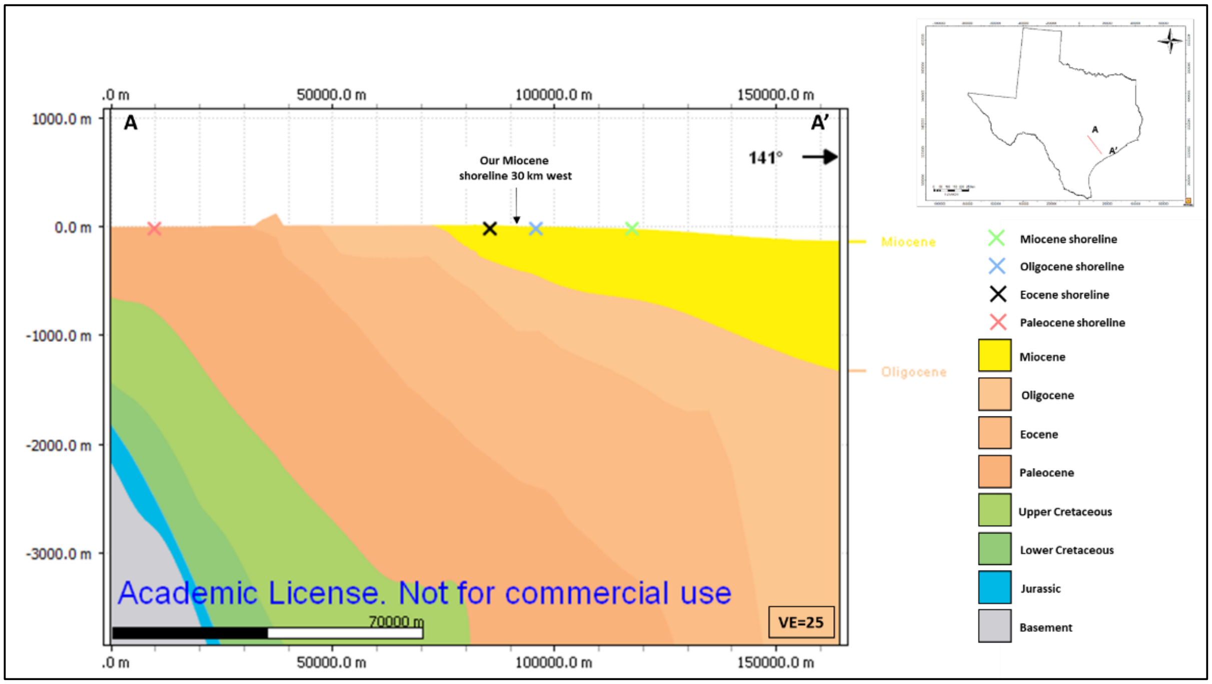

Figure 31. Model 3 Miocene-Pliocene boundary. *Cross-section showing Miocene-Pliocene boundary after decompaction of Quaternary and Pliocene sediments. For this model we used 215 Ma for rifting age, 50 Ma for syn-rift duration and 60 km for elastic thickness. These parameters apply for figures 31 to 35. Refer to table 1 and figure 25 for the results.*

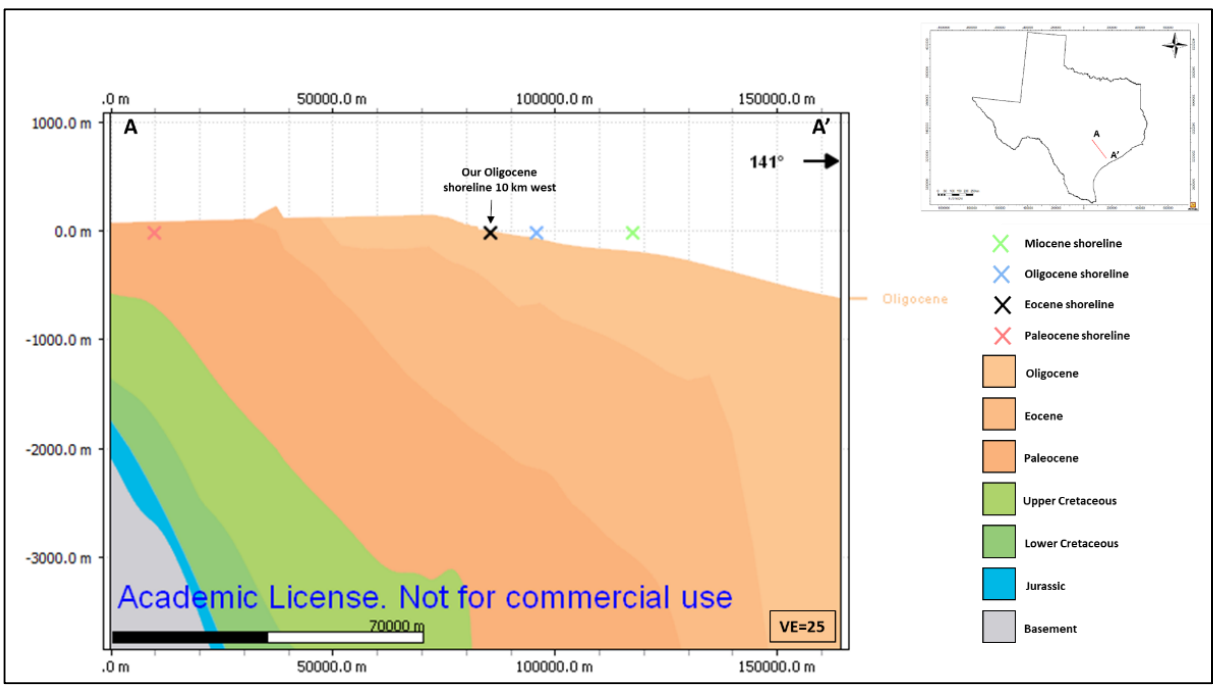

Figure 32**. **Model 3 Oligocene-Miocene boundary. *Cross-section showing Oligocene-Miocene boundary after decompaction of Miocene sediments.*

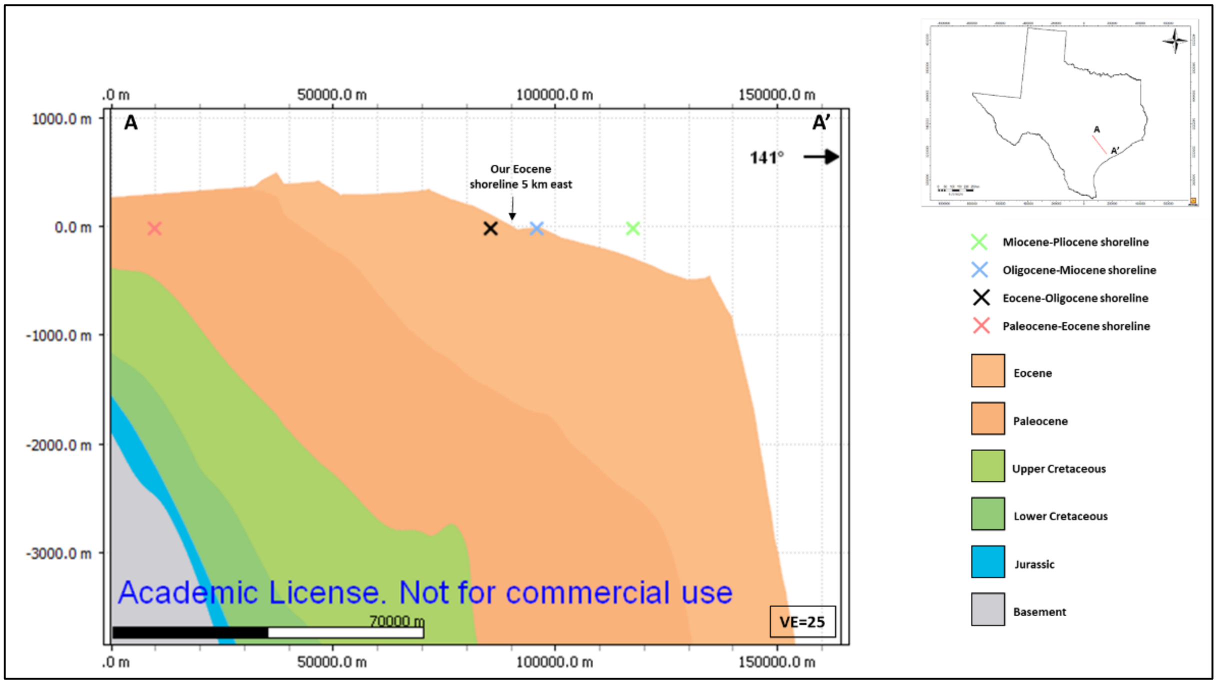

***Figure 33. Model 3 Eocene-Oligocene boundary**. Cross-section showing Eocene-Oligocene after decompaction of Oligocene sediments.*

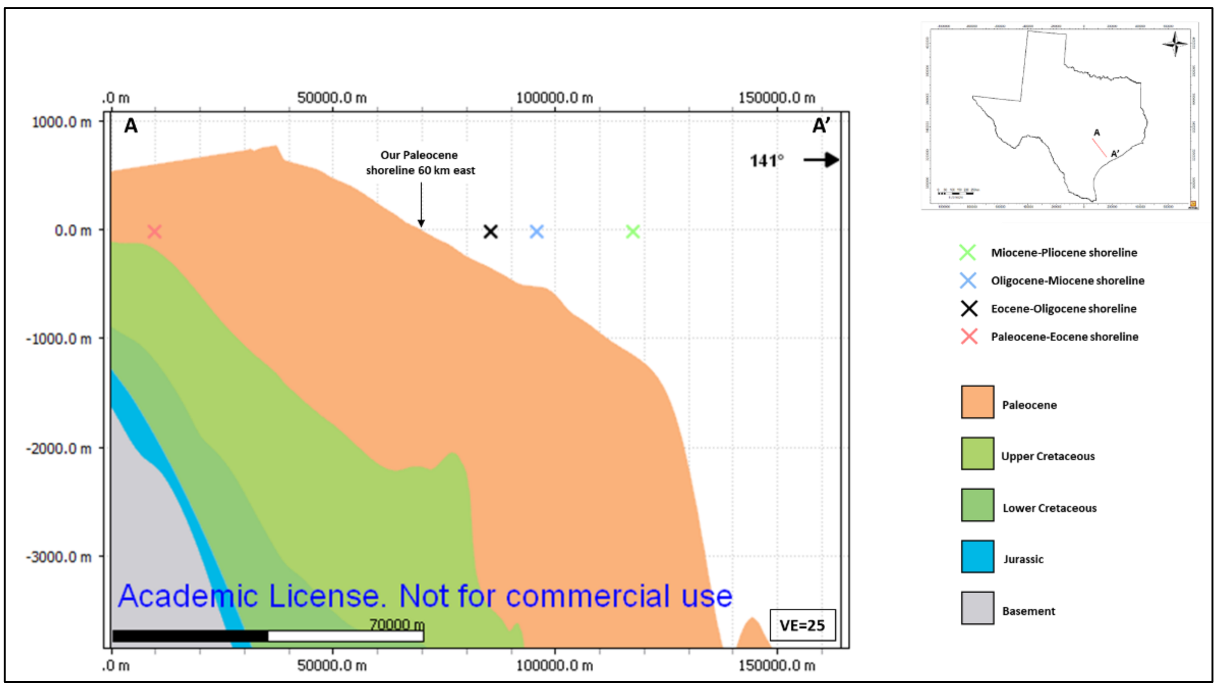

***Figure 34. Model 3 Paleocene-Upper Cretaceous boundary.** Cross-section showing Paleocene-Eocene boundary after decompaction of Eocene sediments.*

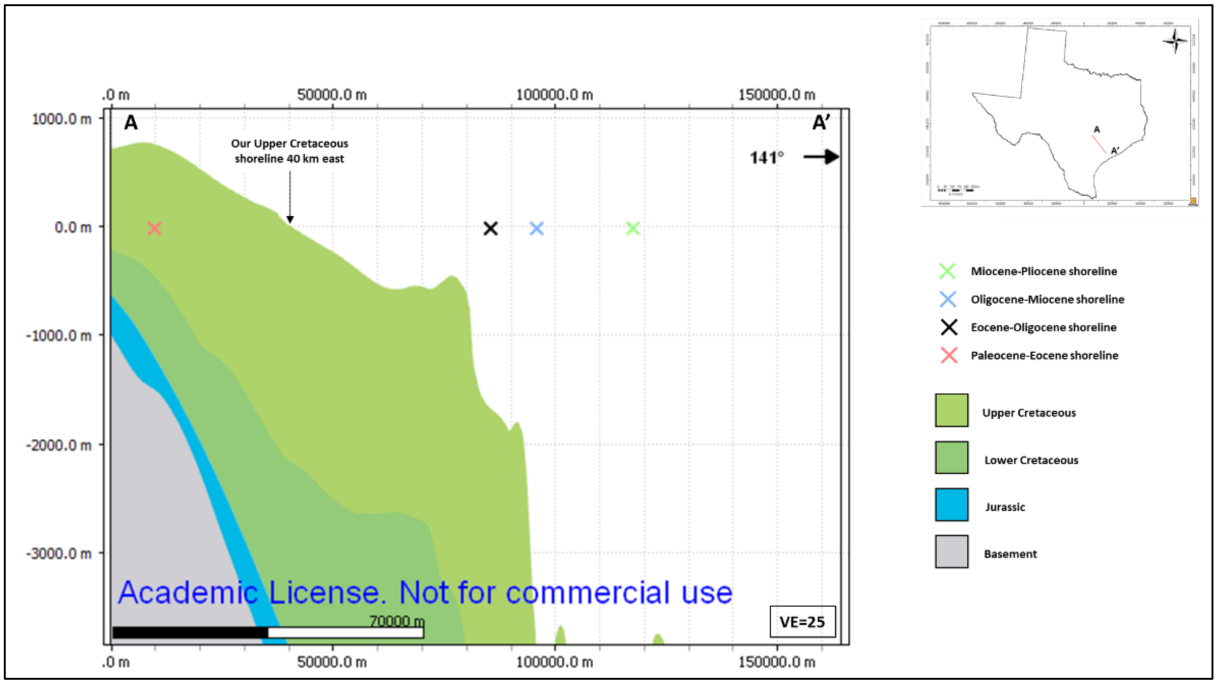

Figure 35. Model 3 Upper Cretaceous-Paleocene boundary. *Cross-section showing Upper Cretaceous-Paleocene boundary after decompaction of Paleocene sediments.*

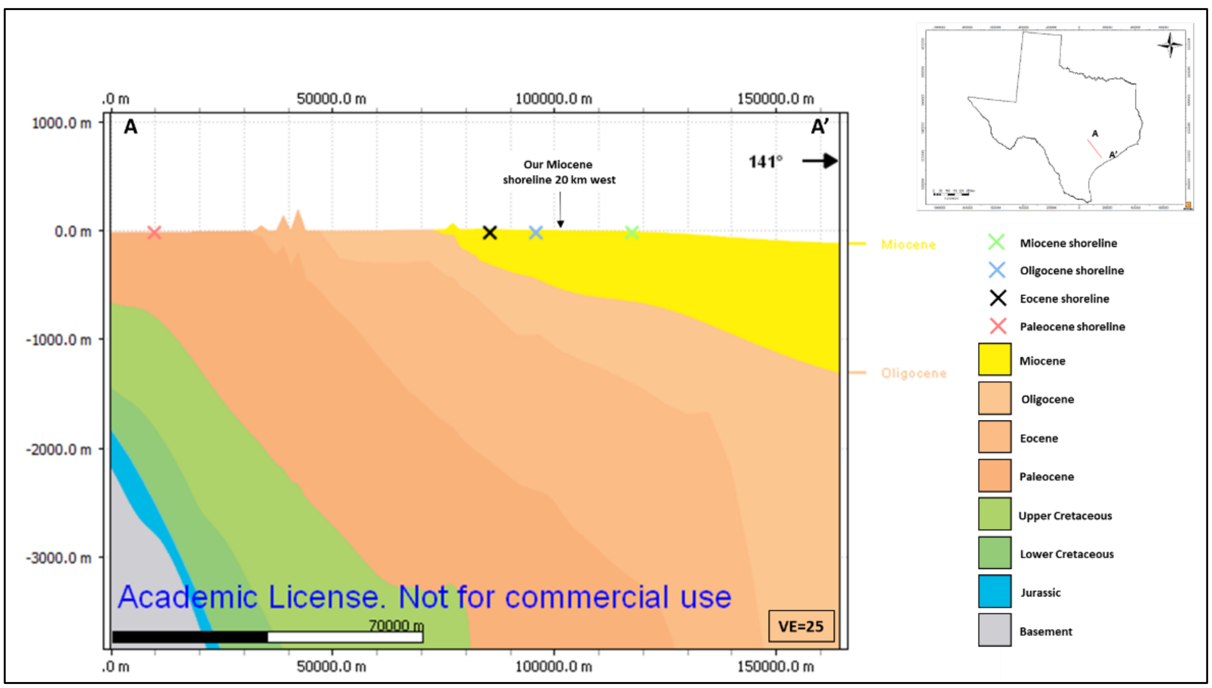

Figure 36. Model 4 Miocene-Pliocene boundary. *Cross-section showing Miocene-Pliocene boundary after decompaction of Quaternary and Pliocene sediments. For this model we used 215 Ma for rifting age, 0 Ma for syn-rift duration and 15 km for elastic thickness. These parameters apply for figures 36 to 40. Refer to table 1 and figure 25 for the results.*

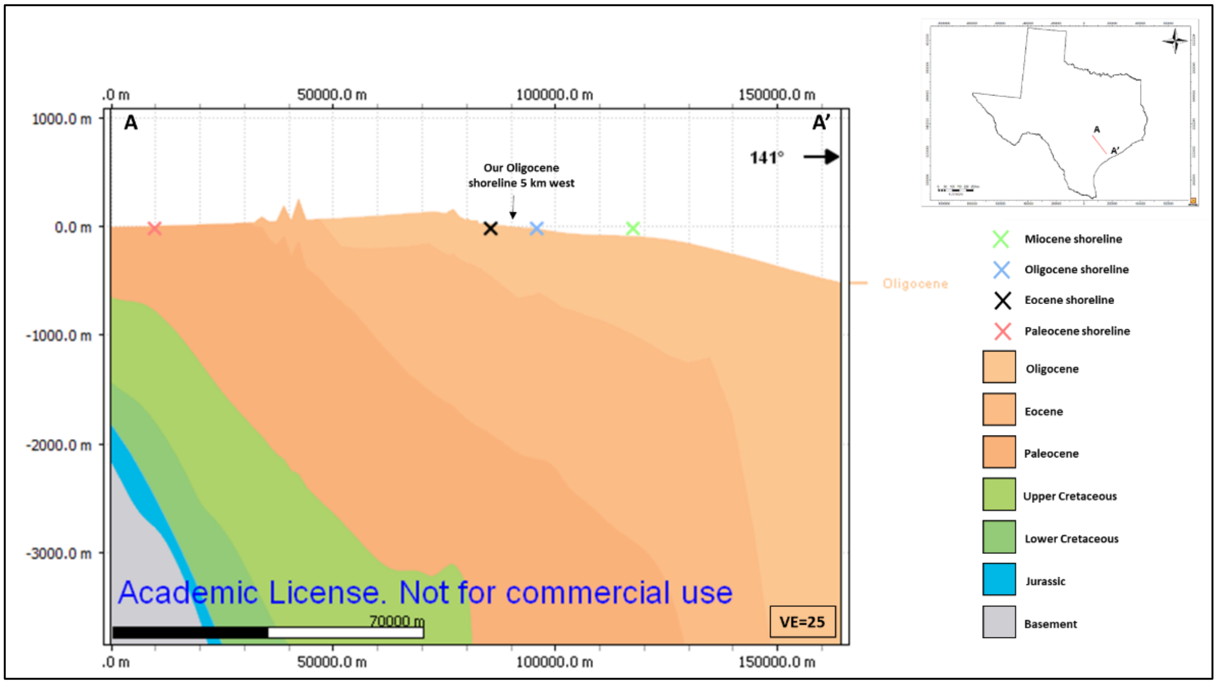

Figure 37. Model 4 Oligocene-Miocene boundary*. Cross-section showing Oligocene-Miocene boundary after decompaction of Miocene sediments.*

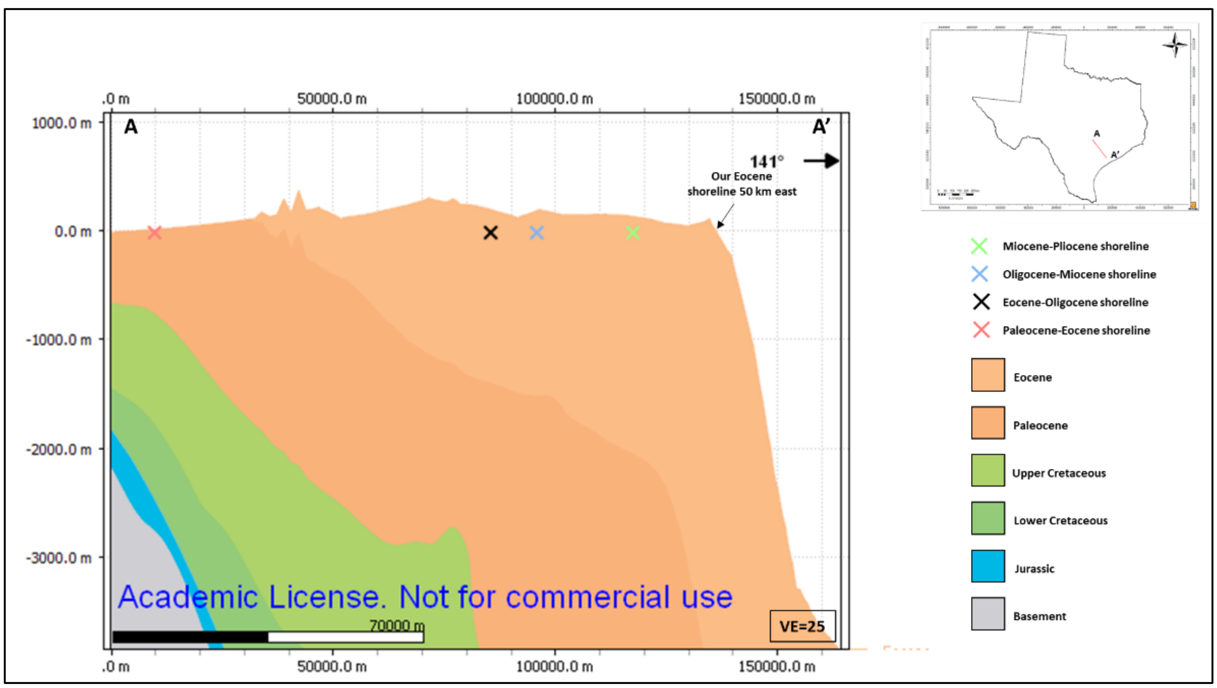

Figure 38. Model 4 Eocene-Oligocene boundary. *Cross-section showing Eocene-Oligocene after decompaction of Oligocene sediments.*

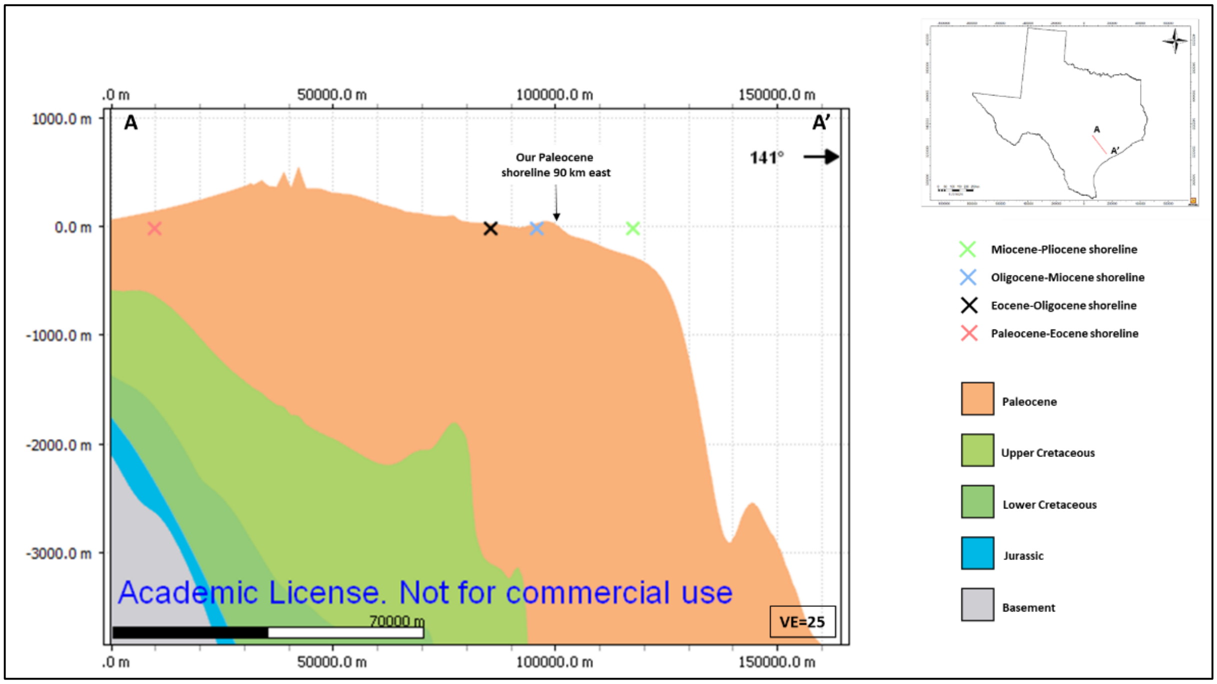

Figure 39. Model 4 Paleocene-Eocene boundary*. Cross-section showing Paleocene-Eocene boundary after decompaction of Eocene sediments.*

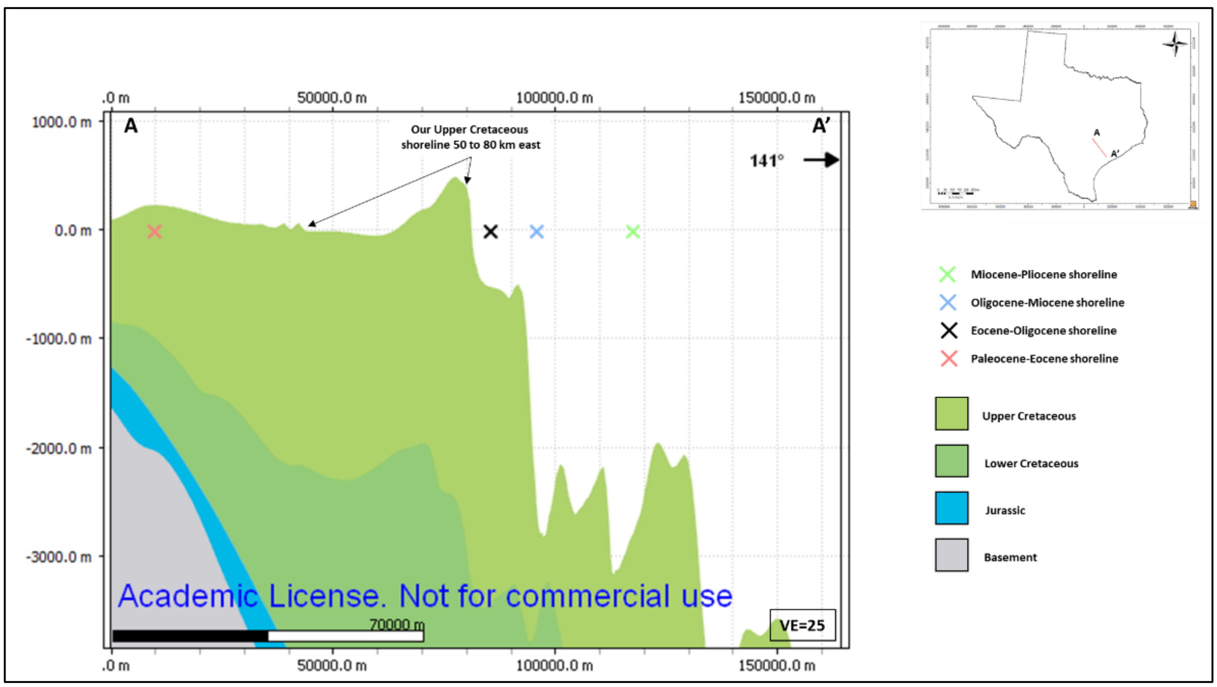

Figure 40. Model 4 Upper Cretaceous-Paleocene boundary. *Cross-section showing Upper Cretaceous-Paleocene boundary after decompaction of Paleocene sediments.*

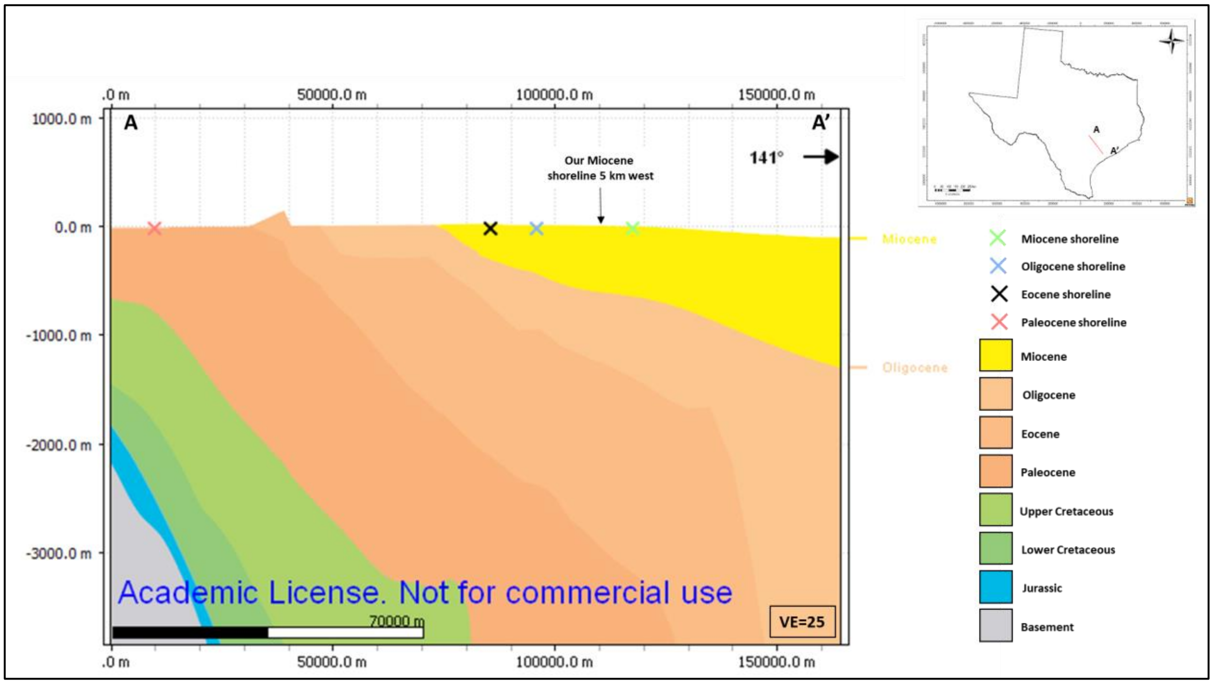

Figure 41. Model 5 Miocene-Pliocene boundary. *Cross-section showing Miocene-Pliocene boundary after decompaction of Quaternary and Pliocene sediments. For this model we used 166 Ma for rifting age, 0 Ma for syn-rift duration and 15 km for elastic thickness. These parameters apply for figures 41 to 45. Refer to table 1 and figure 25 for the results.*

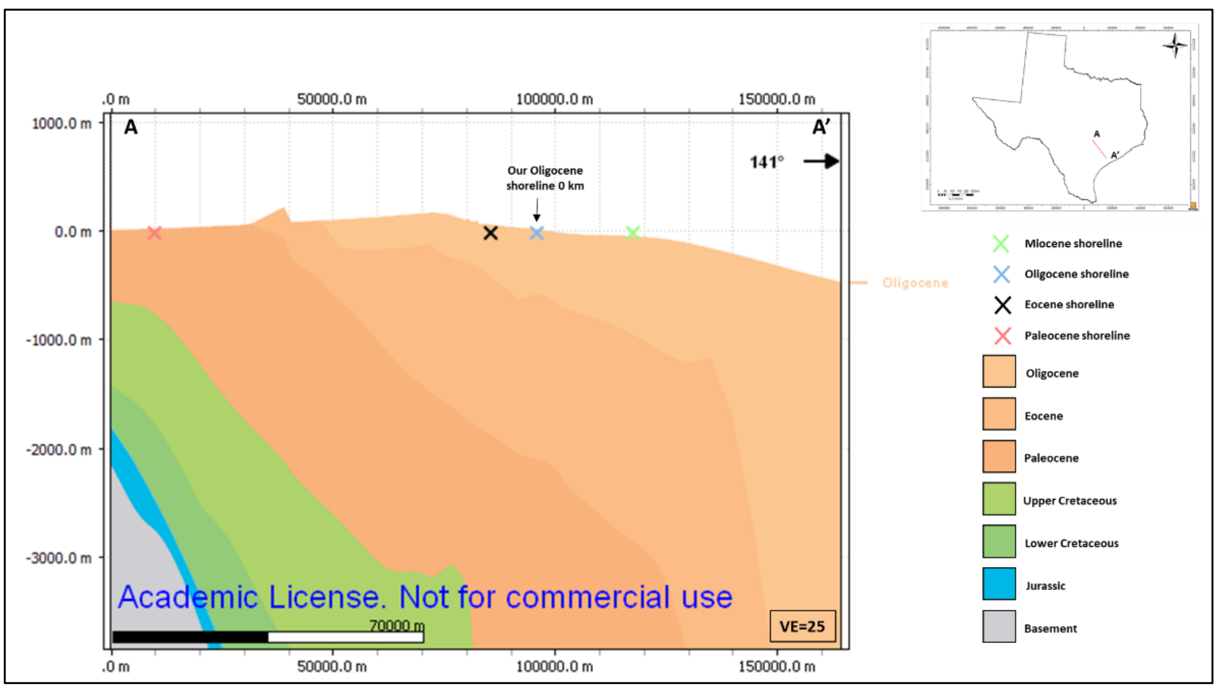

Figure 42. Model 5 Oligocene-Miocene boundary. *Cross-section showing Oligocene-Miocene boundary after decompaction of Miocene sediments.*

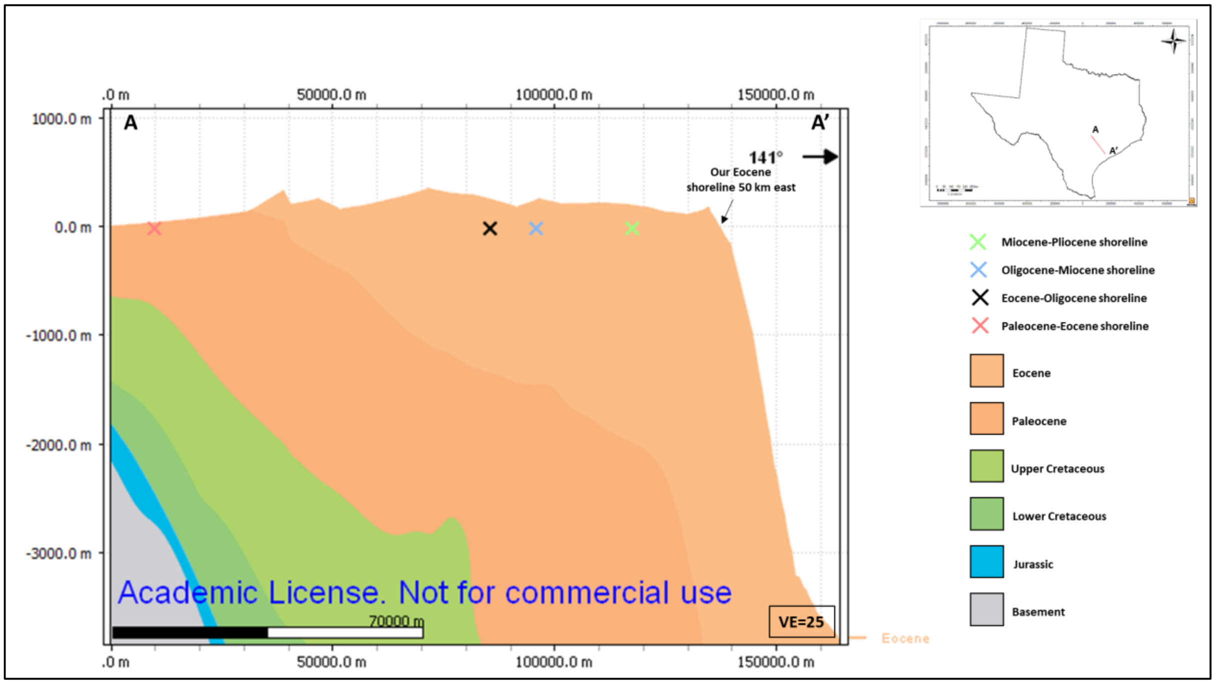

Figure 43. Model 5 Eocene-Oligocene boundary*. Cross-section showing Eocene-Oligocene after decompaction of Oligocene sediments.*

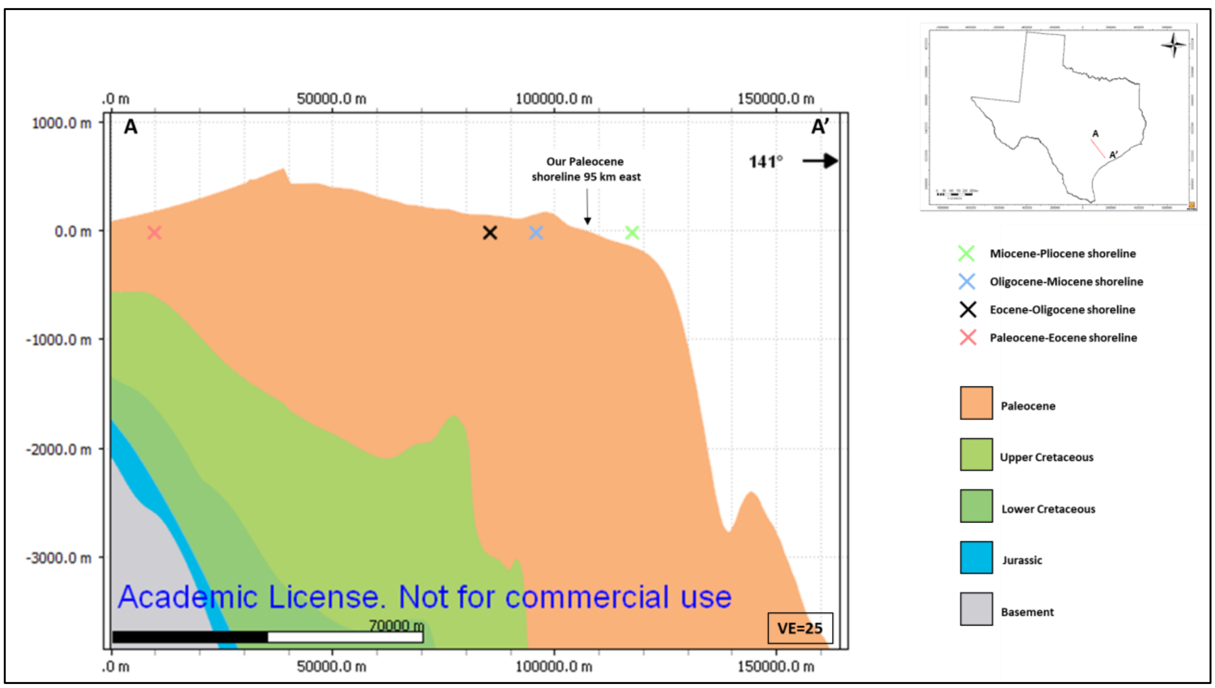

Figure 44. Model 5 Paleocene-Eocene boundary. *Cross-section showing Paleocene-Eocene boundary after decompaction of Eocene sediments.*

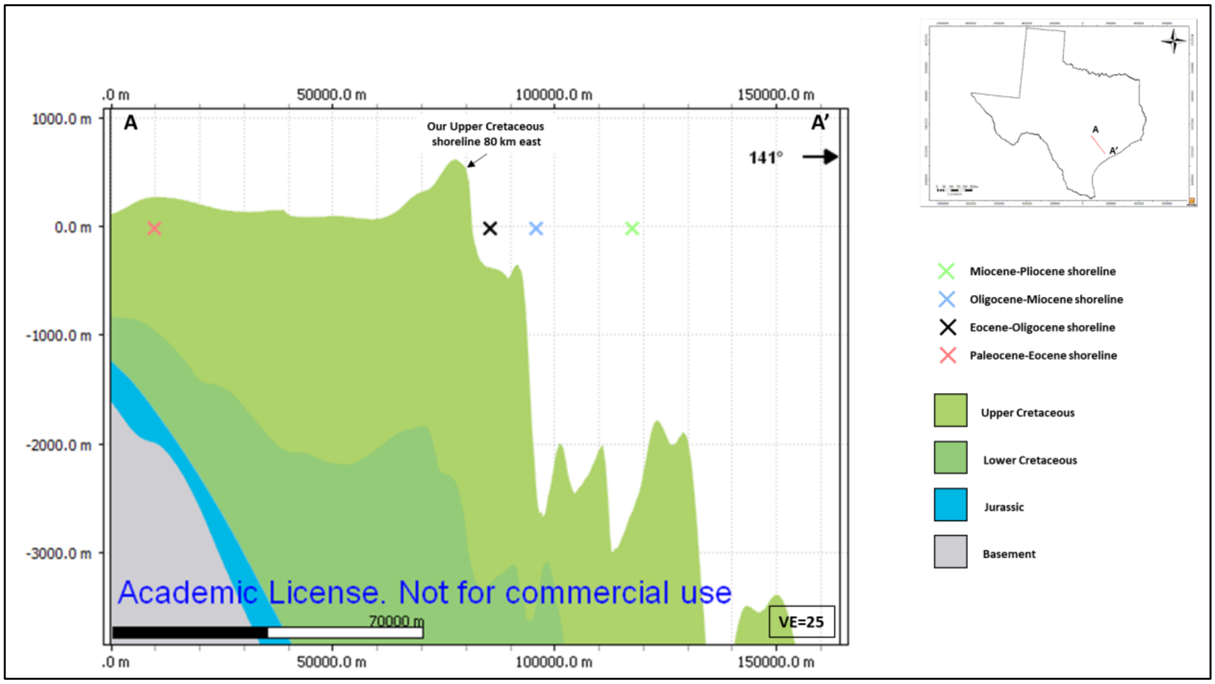

Figure 45. Model 5 Upper Cretaceous-Paleocene boundary. *Cross-section showing Upper Cretaceous-Paleocene boundary after decompaction of Paleocene sediments.*

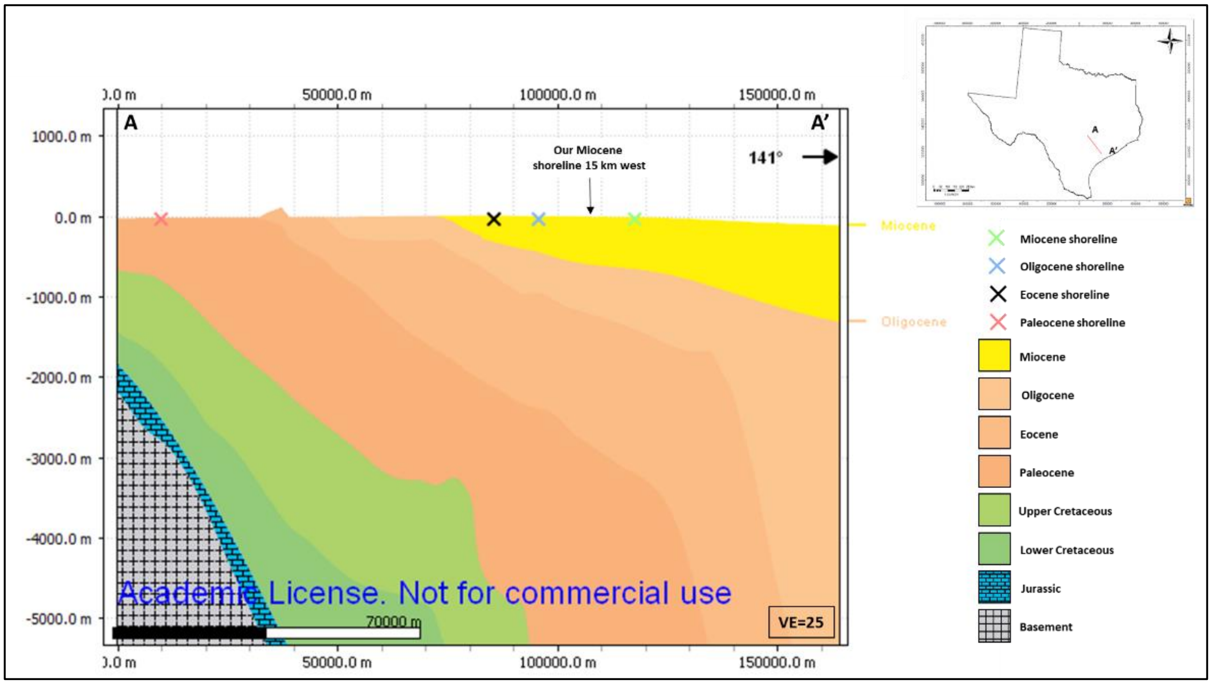

Figure 46. Model 6 Miocene-Pliocene boundary. *Cross-section showing Miocene-Pliocene boundary after decompaction of Quaternary and Pliocene sediments. For this model we used 215 Ma for rifting age, 50 Ma for syn-rift duration and 15 km for elastic thickness and 20% uncertainty for shale values. These parameters apply for figures 46 to 50. Refer to table 1 and figure 25 for the results.*

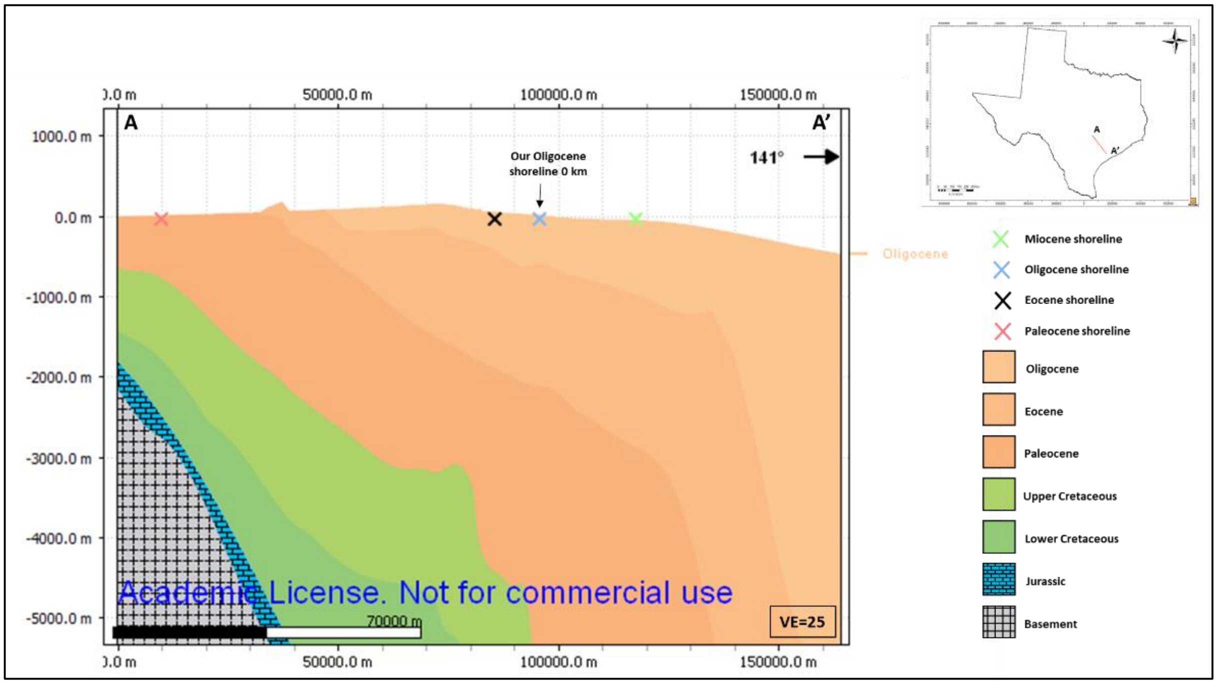

Figure 47. Model 6 Oligocene-Miocene boundary*. Cross-section showing Oligocene-Miocene boundary after decompaction of Miocene sediments.*

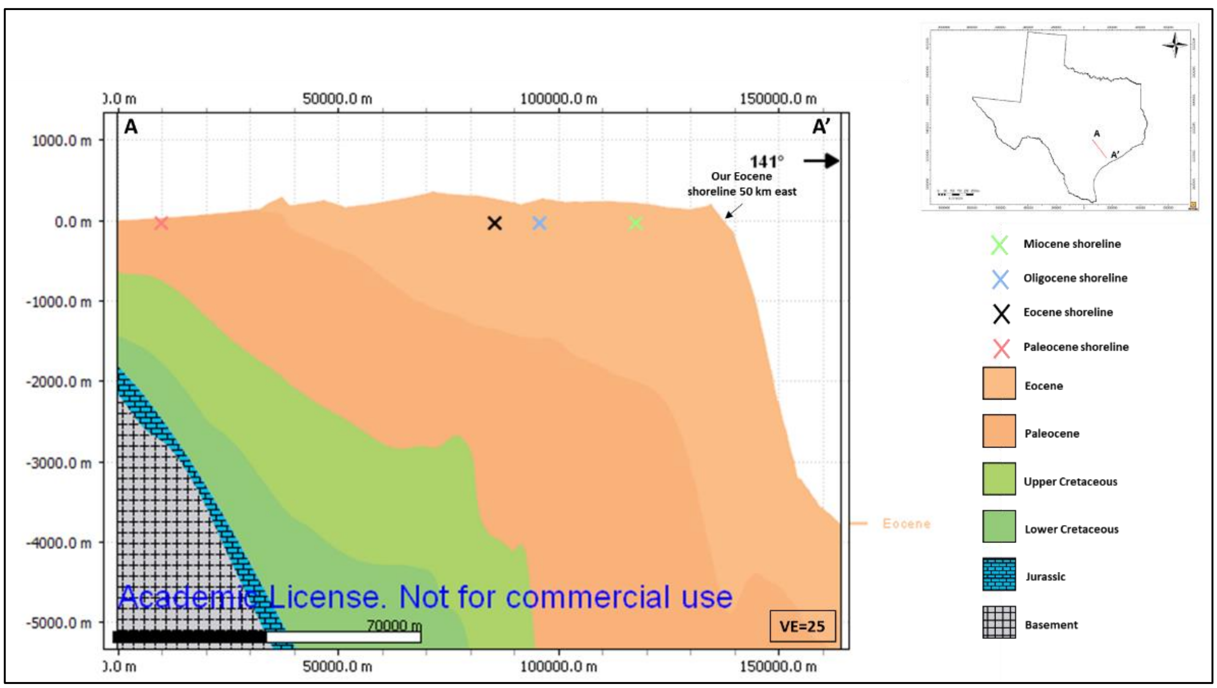

Figure 48. Model 6 Eocene-Oligocene boundary. *Cross-section showing Eocene-Oligocene after decompaction of Oligocene sediments.*

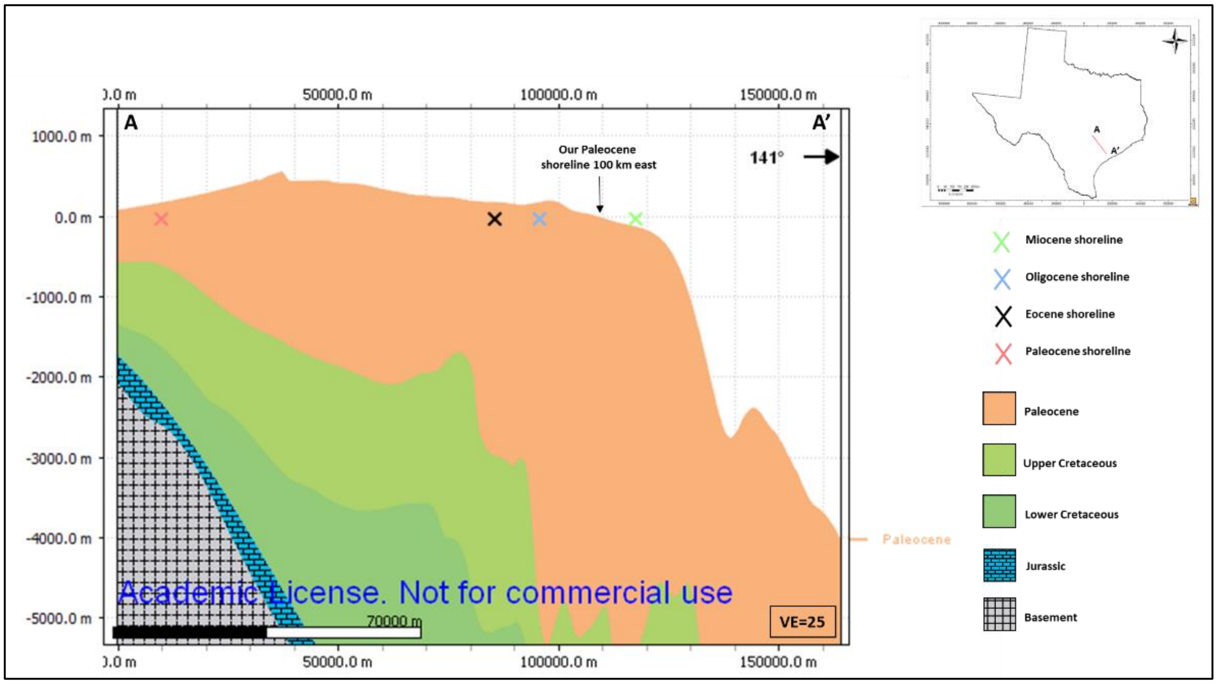

Figure 49. Model 6 Paleocene-Eocene boundary*. Cross-section showing Paleocene-Eocene boundary after decompaction of Eocene sediments.*

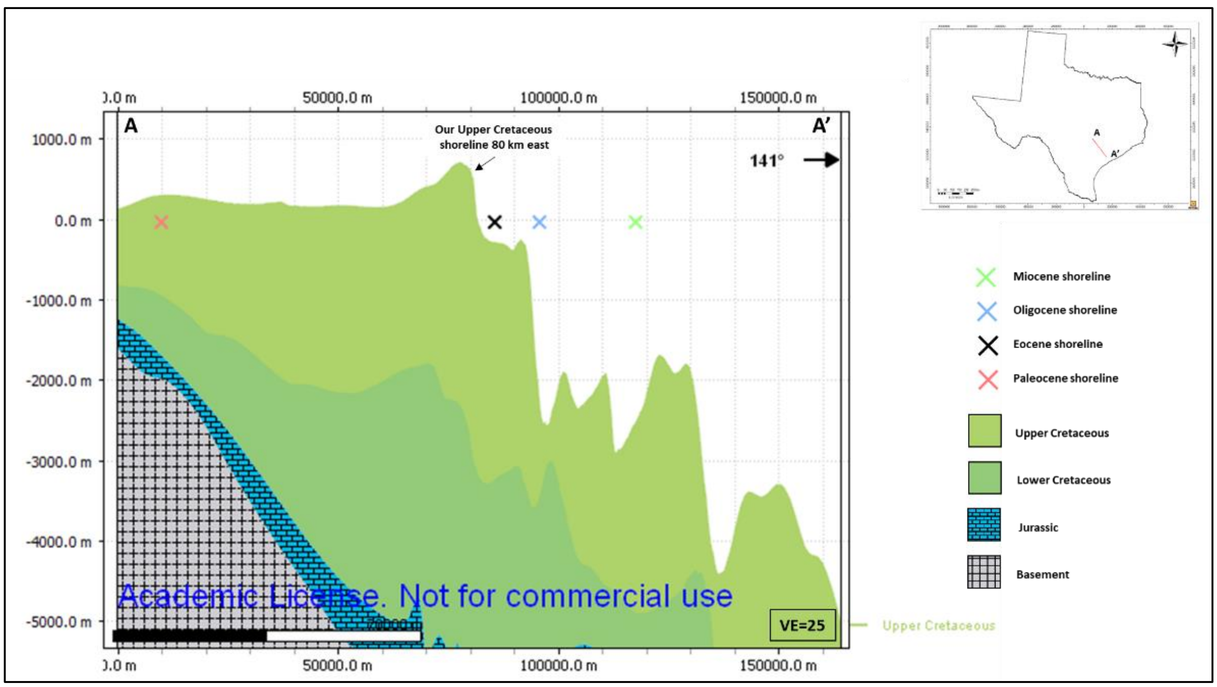

Figure 50. Model 6 Upper Cretaceous-Paleocene boundary. *Cross-section showing Upper Cretaceous-Paleocene boundary after decompaction of Paleocene sediments.*

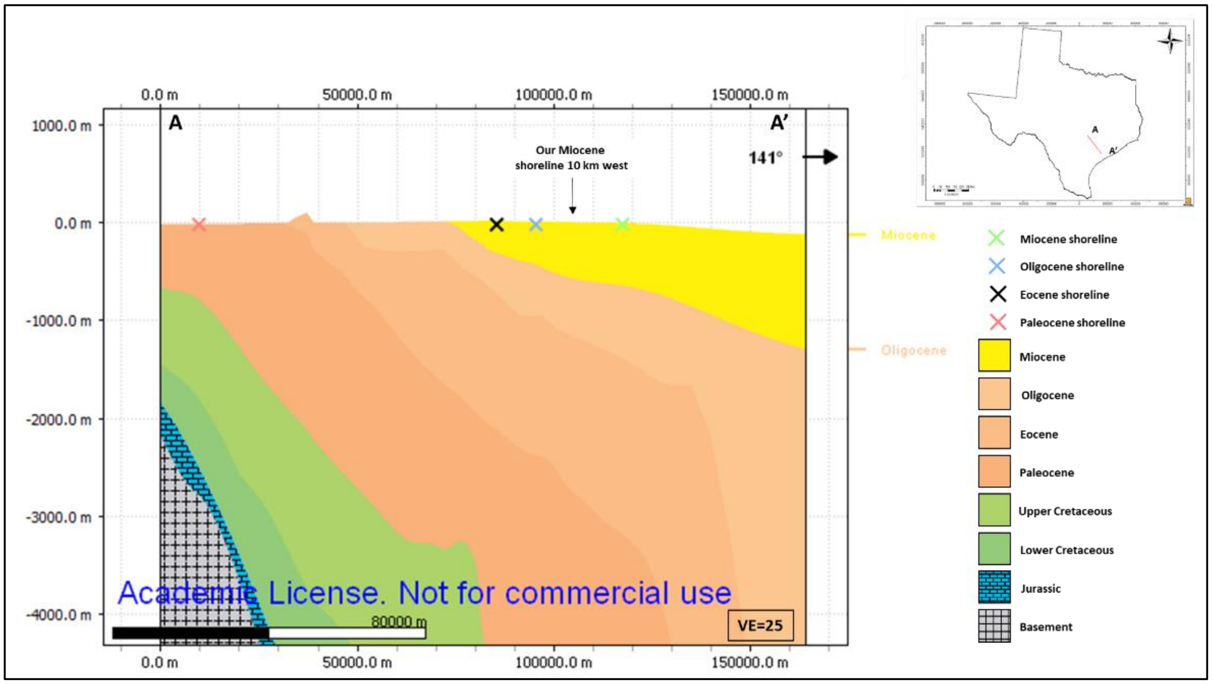

Figure 51. Model 7 Miocene-Pliocene boundary. *Cross-section showing Miocene-Pliocene boundary after decompaction of Quaternary and Pliocene sediments. For this model we used 215 Ma for rifting age, 50 Ma for syn-rift duration and 15 km for elastic thickness and 20% uncertainty for limestone values. These parameters apply for figures 51 to 55. Refer to table 1 and figure 25 for the results.*

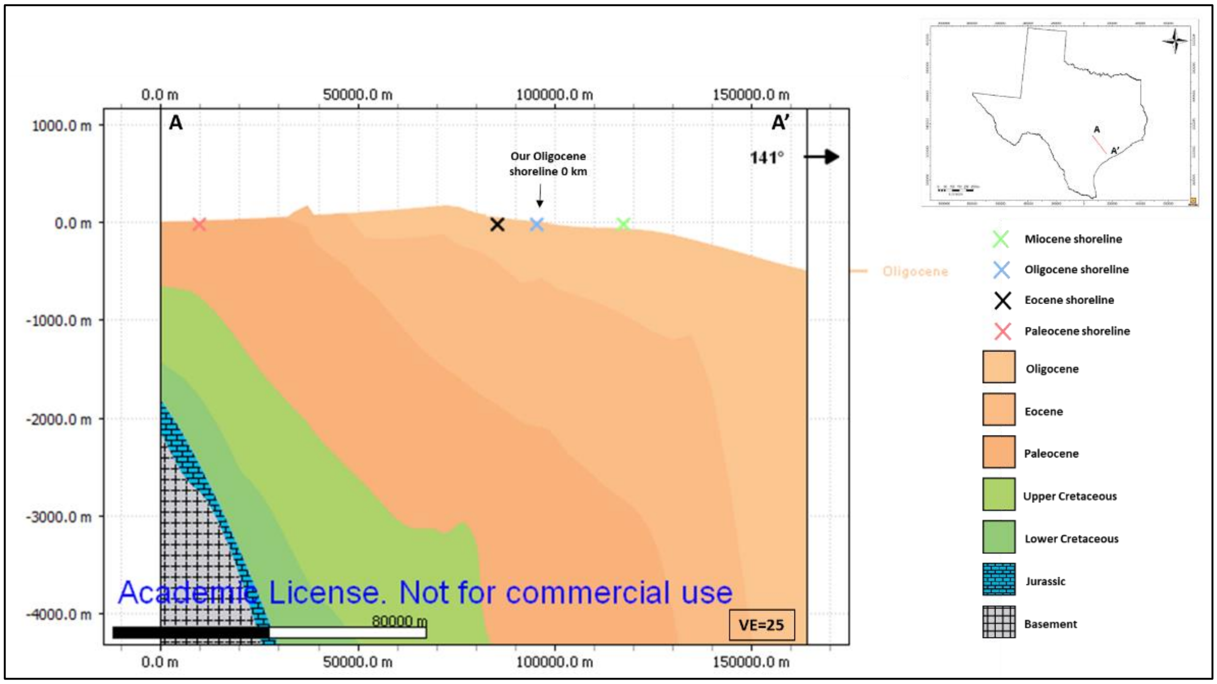

Figure 52. Model 7 Oligocene-Miocene boundary. *Cross-section showing Oligocene-Miocene boundary after decompaction of Miocene sediments.*

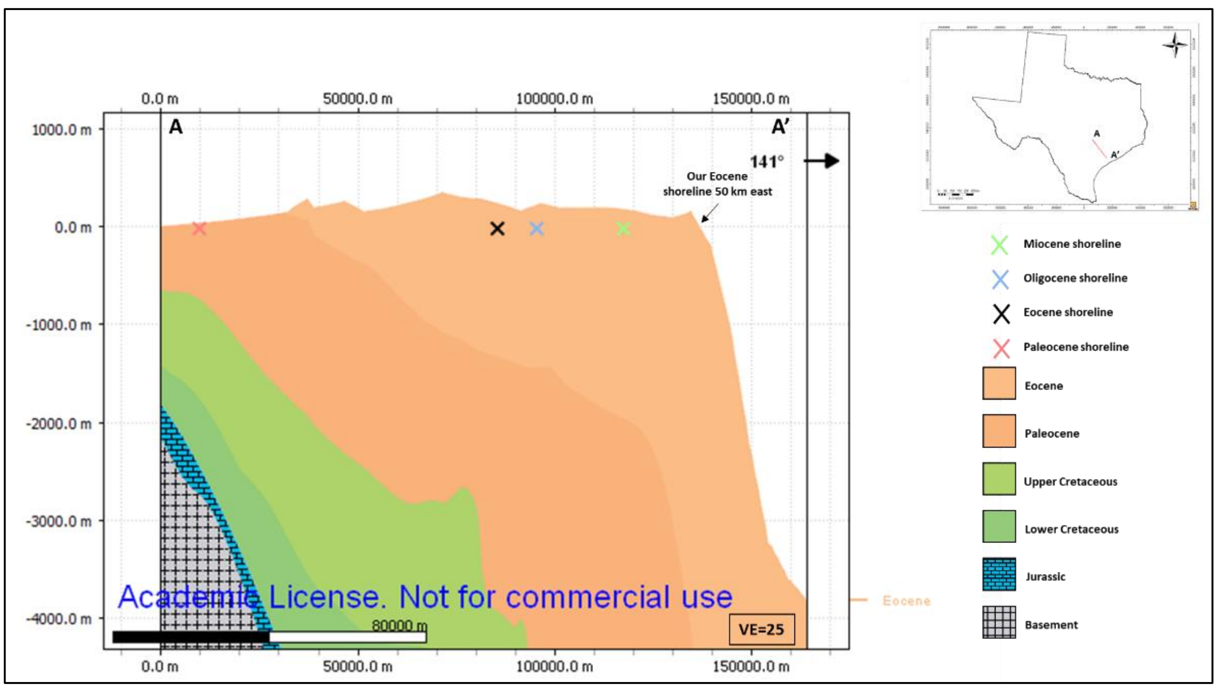

Figure 53. Model 7 Eocene-Oligocene boundary. *Cross-section showing Eocene-Oligocene after decompaction of Oligocene sediments.*

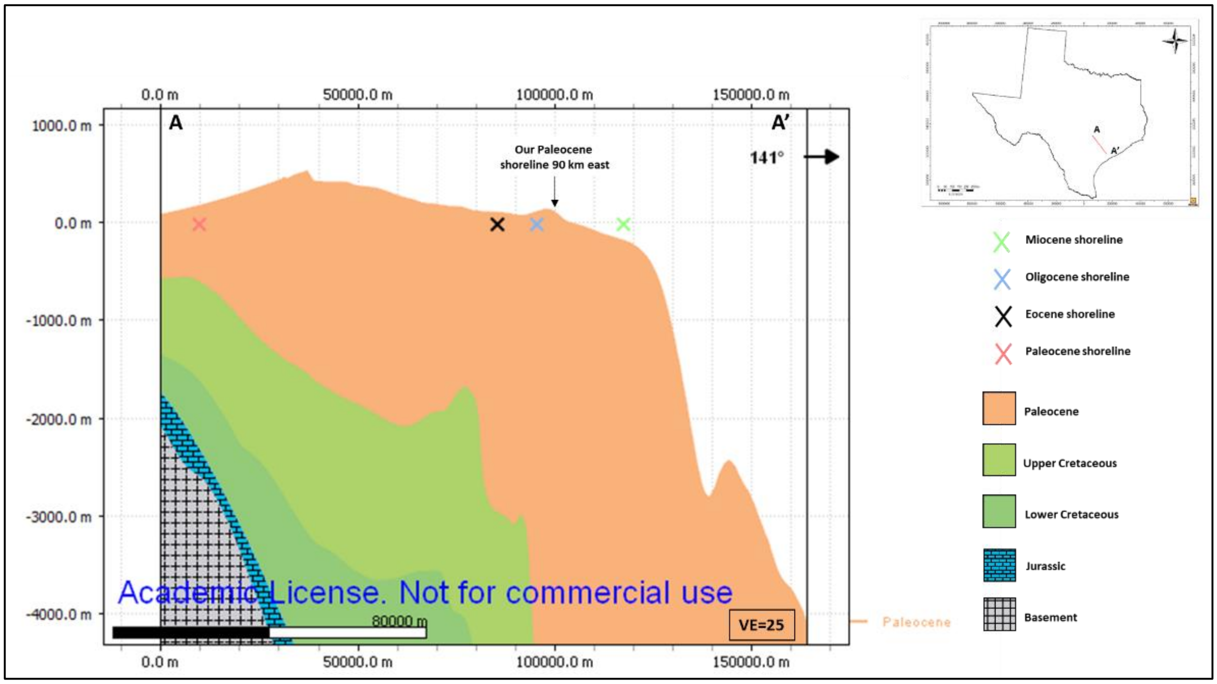

Figure 54. Model 7 Paleocene-Eocene boundary. *Cross-section showing Paleocene-Eocene boundary after decompaction of Eocene sediments.*

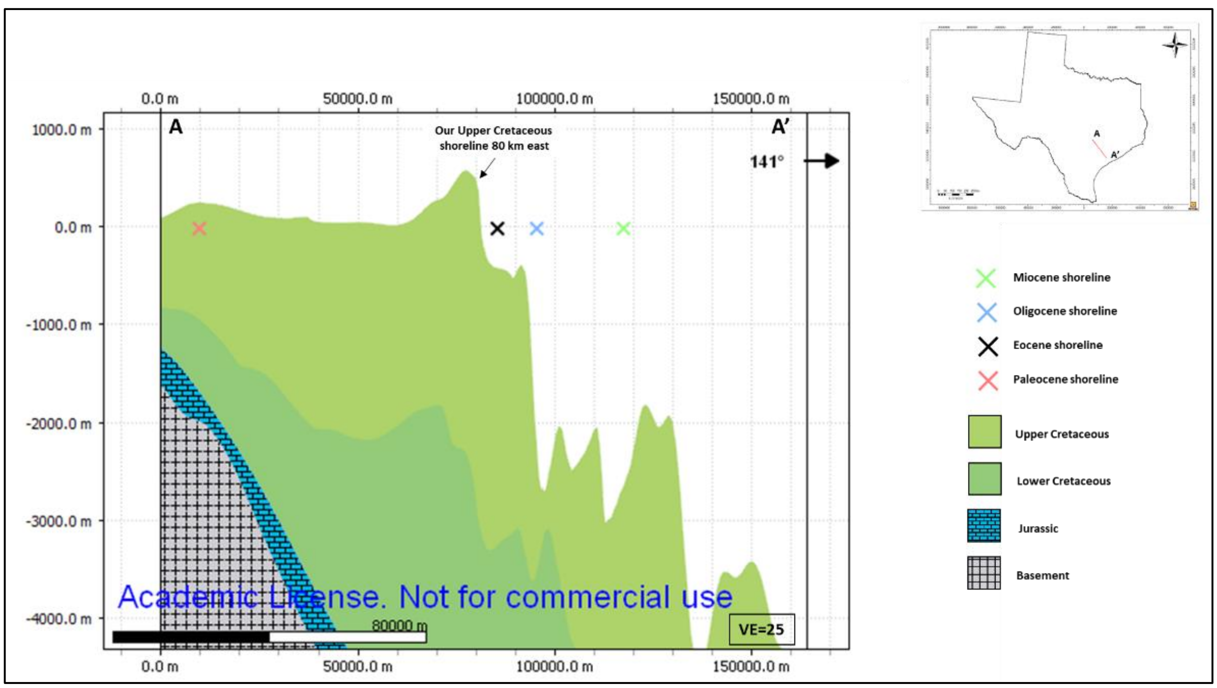

Figure 55. Model 7 Upper Cretaceous-Paleocene boundary. *Cross-section showing Upper Cretaceous-Paleocene boundary after decompaction of Paleocene sediments.*